



**Politecnico  
di Torino**

Politecnico di Torino

Corso di Laurea Magistrale in Ingegneria Biomedica  
A.a. 2020/2021

**Data analysis and model development for a photonic  
interrogation platform for cancer chemotherapy  
optimization using power spectrum analysis of  
sub-cellular dynamics**

Relatori:  
Tuszynski Jacek Adam  
Dogariu Aristide

Candidato:  
Chierici Francesco

*To my father,  
always in my heart.*

## **ACKNOWLEDGMENTS**

Firstly, I would like to thank my supervisor, Prof. Jack Tuszynski from Politecnico di Torino, and my co-supervisor, Dr. Aristide Dogariu from University of Central Florida, for allowing me to do this project in the USA during these difficult times.

Thanks to the other members of the Templeton project: Dr. A. Kalra, Dr. S. Hameroff, Dr. R. Penrose, Dr. G. Scholes, Dr. T. Craddock and Dr. B. MacIver, for giving me the possibility to work with them.

Thanks to Amy Perry of CREOL department and Zack Salloum of UCF Global for helping me in organizing this experience.

Thanks to Ruitao for the help during the project, to Jose Rafael for his feedback and to Mahed, Cristian, Shubham, Mahdi, Zhean, Pedro and Sohila, for all the knowledge they shared with me during these months.

Thanks to Piergiuseppe Vinai, whose advice during all these months abroad allowed me to fully live this experience.

Thanks to Nadine for this year together, for having encouraged me to try to organize this project when I thought it was impossible and for the effort of being separated during these months.

Thanks to all my friends, in particular Michele, Lorenzo and Valentina, for their support during these years and for the moments together, and thanks to Luca and Elisa for our adventures at Politecnico di Torino.

Thanks to my enlarged family: my sister Beatrice, Gabriella and Beatrice for the support and the advices during these years and during this project.

Finally, thanks to my mother Cristina for the support all over my life and for giving me the possibility to study and to realize this dream.

# SUMMARY

1	INTRODUCTION .....	2
1.1	Project description .....	2
1.2	Project significance.....	3
1.3	Tumor and cancer overview.....	6
1.4	Microtubules overview.....	10
2	EXPERIMENTS.....	18
2.1	Experimental procedure.....	18
2.1.1	<i>Normal and cancerous prostate cells</i> .....	18
2.1.2	<i>Chinese Hamster Ovary (CHO) cells</i> .....	19
2.1.3	<i>CHO cells treated with Nocodazole</i> .....	19
2.2	Experimental setup .....	21
2.3	Coherence-gated DLS .....	24
3	POWER SPECTRA ANALYSIS.....	27
3.1	Theoretical remarks.....	27
3.2	Procedure .....	29
4	POWER SPECTRA RESULTS .....	31
4.1	Prostate cells .....	31
4.2	CHO cells monitoring.....	33
4.3	CHO cells with Nocodazole.....	35
4.1.1	<i>Experiment 1</i> .....	35
4.1.2	<i>Experiment 2</i> .....	40
4.1.3	<i>Experiment 3</i> .....	45
5	CONCLUSIONS .....	49
	APPENDIX 1: TUBULIN POLYMERIZATION MODEL IN VITRO .....	52
	APPENDIX 2: ORDERED WATER SYSTEM AROUND MICROTUBULES .....	57
	REFERENCES .....	74

# 1 INTRODUCTION

## 1.1 Project description

The aim of this project is to propose a possible new platform for cancer therapy optimization based on Dynamic Light Scattering (DLS), a non-invasive, low-intensity photonic interrogation technique. Firstly, the system is used to investigate properties of different cell lines without administering drugs to see differences in cell lines and cell states as a proof of their sensitivity with respect to cellular dynamics. Afterwards, DLS is used to investigate cancer cells under an incrementally-increased dose delivery of a therapeutic agent in order to precisely determine its apoptosis-inducing concentration. The platform takes advantage of nano-scale technology and DLS in order to measure the cell dynamics in real time as function of drug dose, ranging from pM to mM, and to obtain the dose-response profile. This allows to better understand the drug efficacy, its side effects and the subcellular dynamics, possibly helping the development of more patient specific therapies because both dose determination and drug administration scheduling can be optimized with this methodology.

Data are taken from experiments performed at CREOL labs of University of Central Florida (UCF) and analyzed using power spectra estimations and micro rheology theory, which provide information on the local cellular properties and internal dynamics. The analysis of the internal dynamics changes induced by drugs, taking into account their known effects on cellular components, is also carried out because these changes are hypothesized to be a measure of the drug's efficacy.

After an introduction focused on this project significance, tumor and cancer characteristics and a microtubules overview, this report will describe the experiments performed and the theoretical basis for the data analysis. Experimental results are then presented and conclusions will be drawn. Finally,

two appendices on microtubules polymerization and the ordered water system around them are included to give insights into environmental effects on cellular dynamics.

## **1.2 Project significance**

Cancer is one of the most important leading causes of death of our time: in 2020 it was the second leading death cause in the US, responsible for about 600k victims [1]. In addition, cancer cases are expected to increase in the next years [2] principally due to the increase of life expectancy: as can be seen in Figure 1.1 the tumor incidence increases significantly after about 40 years for men and 35 for women. This is mainly caused by the fact that tumors originate from genetic damage, which increases over time. In addition to the genetic damage, tumor development can be favored by risk factors related to the lifestyle: smoking, unhealthy diet and obesity are some examples of behaviors or conditions correlated with tumor development [3]. The combination of the long time needed to have a genetic damage and the risk factors explains why cancer incidence is higher in developed countries with respect to the poor ones [4]: higher life expectancy, diet and weight-related risk factors are typical of first world countries, making their cancer rates increasing. Moreover, the number of new cancer cases and related deaths are expected to increase from 18.1 million and 9.1 million worldwide (2018 data) to 29.5 million and 16.4 million (2040 projection), respectively [4].

Lots of intellectual efforts were made and billions of dollars were spent in the last decades to find a cure for this class of diseases which can be treated with different strategies:

- Surgery: the earliest technique, is highly invasive and consists in the removal of the tumor mass. If the removal is not complete, it is possible to have relapse of the cancer or emergence of a secondary cancer elsewhere in the body;

- Chemotherapy: uses drugs to eradicate the cancer cells. The drugs used damage cellular proteins during mitosis in order to block their high rate of replication, so also healthy cells with high replication rates, such as the ones of hair follicles or bone marrow, can be affected by them as side effects;
- Radiotherapy: uses ionizing radiations to damage cellular DNA, prevent its replication and kill it. Commonly used forms of radiation in cancer therapy are X rays, electrons, protons, neutrons and ions, depending on the tumor characteristics. This strategy allows a local and painless treatment but cannot be used for all tumors and sometimes can only be used for palliative purposes. It also commonly leads to side effects due to damage inflicted on normal cells on the path to the tumor or in the vicinity of the tumor cells.
- Thermal therapy: hyperthermia and thermal ablation can be used to treat certain tumors and cancers. In particular hyperthermia can be use alone or in combination with other strategies because it increases radiation sensitivity and tumor perfusion, while ablation can be used to kill some localized tumor portions by inducing necrosis;
- Combined approach: it is composed by the combination of some of the previous strategies, like thermal therapy plus chemo/radiotherapy.

Regarding chemotherapy, the therapeutic progress is hampered by a series of factors:

- Cancer initiation and progression involves about 500 molecular targets, that is almost 1/3 of all molecular targets identified for all human diseases [5];
- Tumors are heterogenous and hence are commonly not composed of a single cell phenotype but instead are best described as a society of malignant cell with different phenotypes [6] and since the typical drug acts only on one phenotype the resistant ones survive;
- The drug resistance phenomenon [7], which is partially due to the previous statement and partially caused by the evolutionary adaptation of cancer cells and their competition against normal cells in a micro-environment not suitable for these ones [8] because it is hypoxic, acidic [9] and lacks proper

organization due to the abnormal proliferation of these cells that can survive without anchoring to the extracellular matrix [10].

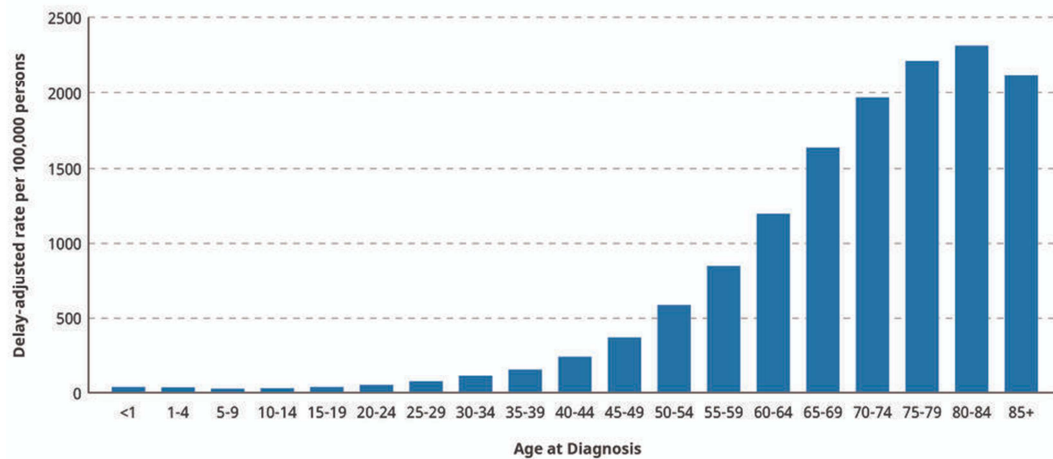


**Figure 1.1:** Cancer incidence per 100,000 people. Picture taken from the National Cancer Institute of the United States: <https://www.cancer.gov/about-cancer/causes-prevention/risk/age>

For all these reasons the improvement of chemotherapy is a challenging endeavor and this project tries to propose a new approach to the problem. The developed platform allows real-time interrogation of the internal structural dynamics over a long duration of time and at an unprecedented level of spatio-temporal resolution and accuracy because the projected time- and frequency-domain resolution provides a deep insight into intra-cellular motions of cells exposed to various cytotoxic agents and their combinations. The approach is based on the fact that internal movements of cellular biomolecules and organelles are manifestations of the cell's energetic state and its "freezing" indicates a transition to Brownian dynamics characteristic of cell death. Precisely determining the transition point to the "freezing" state allows making comparisons between drugs actions on different cancer cells and better understanding side effects on normal ones. In addition to this, the methodology can be used to investigate individual cells as well cell cultures, allowing to determine the significance of statistical averaging as a potential distortion of multimodal distribution of cancer phenotypes in a heterogeneous tumor

environment. Another feature of this approach is that it allows to investigate not only the dynamics of the cytoskeleton but also specific cell components such as mitochondria or motor proteins. This permits to relate the drug to the corresponding intracellular structures affected and thus to improve our knowledge on the drugs' mode of action. Finally, using sub-lethal concentrations of cytotoxic agents on a population of cells, one can investigate drug resistance when surviving cells are exposed to a variety of other drug entities.

In conclusion, this system can become a new bioengineering tool for drug testing as well as for the development of personalized therapies since it could be used on biopsied patient samples. The technology can be adapted to clinical use by performing tests on patient tissue before choosing a therapeutic regime in order to determine a potential for success of an already FDA-approved drug, an off-labelled drug recommended by the oncologist or a new experimental drug ready for the clinical trial.

### **1.3 Tumor and cancer overview**

Tumor is defined as a mass of tissue that grows in excess and without coordination with respect to normal tissues and remains in this condition even after that the stimuli inducing the process end [11]. Tumors typically originate due to genetic damage: all tumor cells show genetic damage and for a given tumor this damage it is always the same, meaning that all the cells originate from only one damaged mother cell (monoclonal origin). Tumors can be classified in different ways:

- Histological classification [12]: the tumor name identifies the tissue of origin of the proliferative cells. According to this method we have for example carcinomas, gliomas and lymphomas;
- According to their invasive capability we can have benign tumors [13], which cannot invade other tissues, and malignant tumors [14], or cancers, which can invade other tissues;

- TNM classification: TNM is a code used to describe the tumor characteristics in terms of dimension (T), nearby lymph nodes that have cancer (N) and metastases presence (M) [2].
- Grading classification: it reflects the grade of differentiation of the tumor cells. A higher level of differentiation means cells similar to healthy ones and thus a less aggressive disease, while a lower differentiation means the tumor is more aggressive [2].

It is important to underline that benign tumors cause pain mainly due to the compression they make on other organs and can lead to more severe problems when they compress vital organs like brain. Moreover, they show cells similar to healthy ones (low grade number) and do not diffuse far from their area of origin, so they do not form metastases. They are easier to deal with and are characterized by a low grade of relapse after removal, but with time, if not treated, some of them can evolve into malignant ones. On the other end, cancer cells are quite different from the healthy ones and the more the de-differentiation is pronounced, i.e. the more they differ with respect to other cells, the more the cancer is aggressive. Cancer cells are different with respect to tumor cells (Figure 1.2) because they present typical extensions similar to tentacles and can diffuse into blood or lymphatic vessels which allows them to reach other organs and attack them: this is how metastases form (Figure 1.3). Finally, since they are more aggressive and can attack different organs, they are also characterized by a high rate of relapse after removal.

Cancer cells behave differently from normal ones, in particular it is possible to identify eight characteristic hallmarks for them [9]:

- Sustaining proliferative signaling;
- Evading growth suppressors;
- Activating invasion and metastases;
- Enabling replicative immortality;
- Inducing angiogenesis;
- Resisting cell death;

- Reprogramming of energy metabolism;
- Evading immune destruction.

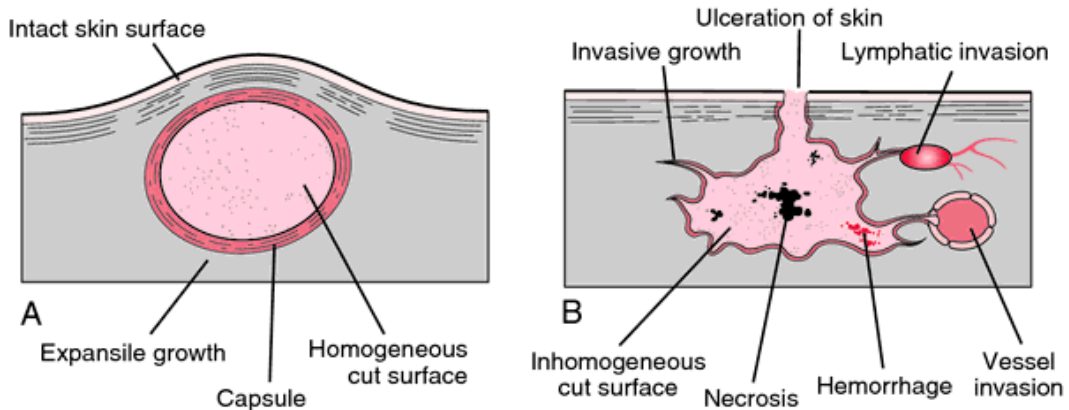


**Figure 1.2:** (A) Benign tumor representation. Note the capsule defining the tumor border and the absence of spreading. (B) Cancer representation. Note the absence of a capsule and the spreading cells. Picture taken from Damjanov, 2000.

All these behaviors are possible if the cell signaling is altered: growth factors, among other molecules, are probably overexpressed while genes limiting cell proliferation and inducing apoptosis are inhibited [9]. In a similar way, necrosis, immortality, inflammatory response and angiogenesis are altered [9]. Regarding metastases formation, the process is usually described as a cascade of events in which cells that can survive all the events start replicating in a different site from the original location [15] and its biochemical mechanisms are still not completely understood. One of the most famous cancer cell behaviors is the so-called “Warburg effect”: cells switch their major energy production from aerobic respiration to glycolysis even if they are not in hypoxic condition, probably due to mitochondrial abnormal activity [16].

As stated previously tumors and cancers can have different differentiation grades, so it is possible to distinguish among some cellular types in them. In addition to cancer cells, which originate the disease, cancer stem cells [17], endothelial cells [18], pericytes [19], immune inflammatory cells [20] and cancer-associated fibroblast [9] can be found, meaning that tumor stroma is a complex

microenvironment more than just an aggregate of pathological cells. The stroma can therefore give a lot of information and provide potential targets for drugs.

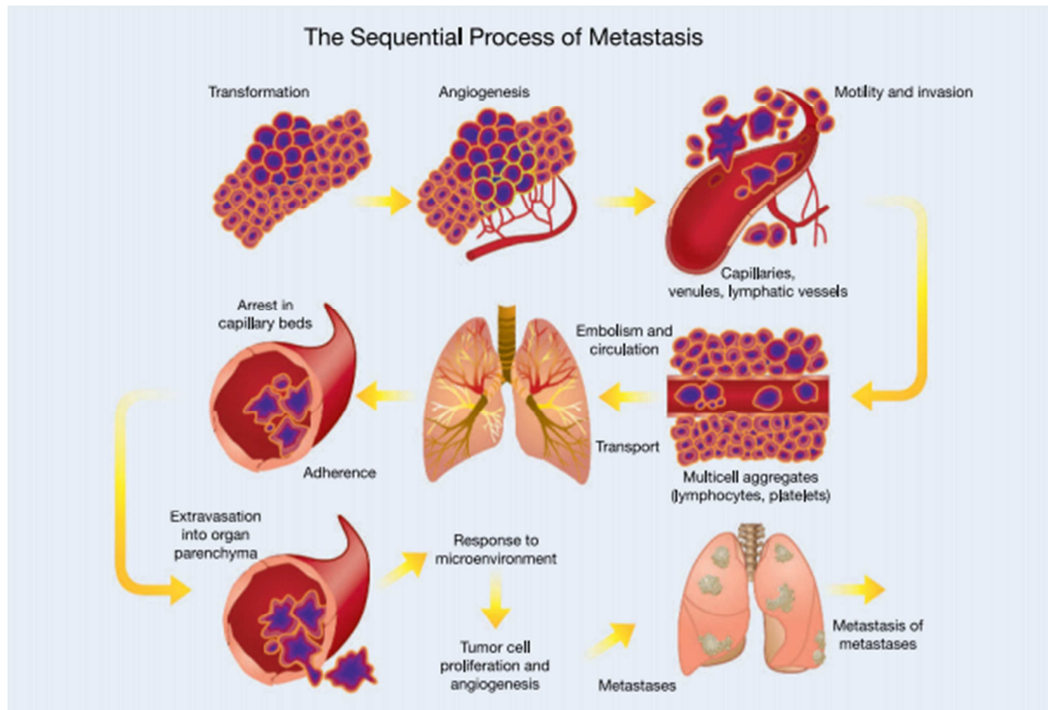


**Figure 1.3:** The sequential process of metastasis. Figure taken from ref. [15].

Tumor cells have a different behavior and microenvironment with respect to healthy ones and as a consequence tumor region develops the following characteristics, that have been studied extensively in order to improve chemotherapy:

- High blood flux but with a chaotic vessel structure;
- Less nutrient diffusion due higher intra-tumor pressure;
- Lower oxygen concentration: hypoxic environment;
- Higher local acidity;
- Different concentrations of proteins and enzymes;
- Enhanced production of reactive oxygen species (ROS).

Chaotic angiogenesis is responsible for the Enhanced Permeability and Retention Effect (EPR Effect): the disorganized vessel growth causes them to have a fenestrated endothelium, which allows accumulation of long-circulating

macromolecules by extravasation [21]. The EPR Effect is of great interest because it could be used for drug delivery with nanoparticles and some attempts were already made in this direction [22].

The higher intra-tumor pressure due to blood and lymphatic vessel abnormalities, interstitial fibrosis and contraction of the matrix [23] is responsible for a reduced amount of nutrients and is also an obstacle to drug delivery because it opposes molecular diffusion towards the tumor.

Tumor hypoxia comes up when  $O_2$  partial pressure falls below a critical value [24] causing a lack of oxygen supply to the cell. Also, this abnormality was studied as a possible target for therapy [25].

The local acidity refers to the tumor extracellular environment, which has a lower pH with respect to the physiological one, while the intracellular environment has higher pH than the healthy one, making the relation between these two environments reversed [26]. This abnormality was used to design pH sensitive nanoparticles to release drugs [27].

The enhanced production of ROS species is responsible for the altered ratio of glutathione (GSH) and glutathione disulfide (GSSG): since GSH is the main antioxidant enzyme in the cell [28], a high GSH/GSSG ratio (typical of healthy cells) indicates a low oxidative stress while a low GSH/GSSG ratio (typical of cancer cells) is related to high stress and pathological conditions, so redox sensitive nanoparticles can be designed [29].

Various drugs have been approved for chemotherapy and a significant amount of them acts on microtubules, which contribute in generating the signal analyzed with the DLS platform, so a description of them is necessary to understand the project and it is provided in the following section.

#### **1.4 Microtubules overview**

Microtubules (MTs) are the main component of the cytoskeleton, a network of protein filaments present in every cell which includes MTs, intermediate filaments and actin filaments and has several functions in the cell. MTs are

hollow cylinders of internal radius 8.4 nm, external radius 12.5 nm and length of some micrometers, usually made of 13 protofilaments of tubulin dimers. Each tubulin dimer is made of one  $\alpha$ - and one  $\beta$ -tubulin subunit: both of them are globular proteins whose mass is approximately 55 kDa, making the dimer a 110 kDa macromolecule of dimensions 4x5x8 nm. Moreover, every tubulin monomer has a 4x1 nm C-terminus tail protruding from it being exposed on the outer surface of the MT. Adjacent protofilaments are not aligned one to the other but they come up in a 3-start helical structure in which each turn of the helix spans 3 tubulin monomers, making  $\alpha$  subunits adjacent to  $\beta$  ones. This organization results in two possible lattices, called A and B lattice [30].

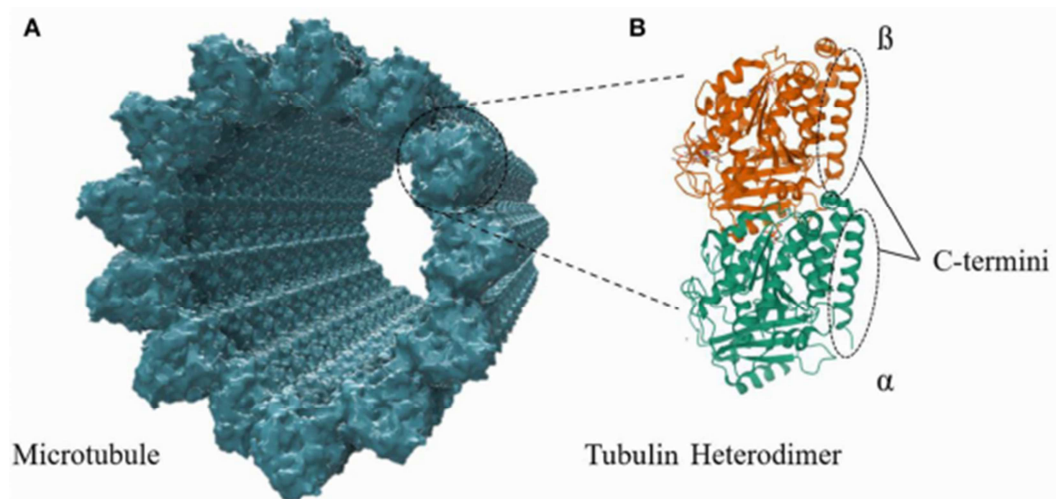


**Figure 1.4:** Structural representation of a microtubule (A) and a tubulin heterodimer (B), both taken from ref. [54].

MT polymerization and depolymerization are complex phenomena involving different steps, alternating between each other and giving rise to what is known as dynamic instability (Figure 1.5). Namely, this is a sequence of stochastic growth and shrinkage periods [31]. MT assembly starts with a nucleation phase [32] in which the  $\gamma$ -tubulin combines with other proteins to form a structure called “ $\gamma$ -tubulin ring” ( $\gamma$ TuRC). The  $\gamma$ TuRC acts as a template for heterodimer polymerization giving binding sites to  $\alpha$ -tubulins of the dimer, allowing the MT to grow in one direction. In this mechanism it is therefore possible to identify a not

growing end in correspondence of the  $\gamma$ TuRC or the exposed  $\alpha$ -tubulin (in vitro), called the Minus (-) End, and a growing end exposing  $\beta$ -tubulins, called the Plus (+) End. The dimer addition requires guanosine-triphosphate (GTP) hydrolysis into guanosine-diphosphate (GDP) of the GTP bounded to the  $\beta$  subunit as an energy source. On the other hand, during depolymerization tubulin heterodimers detach from MT, resulting in its shrinkage or even in a catastrophe in which the MT is completely or almost completely disassembled. Another dynamic behavior observable in MTs, called treadmilling, is the growth at one end balanced by shortening at the other, resulting in an overall null net growth rate [33]. MT dynamics is not completely understood and it is influenced by a lot of features:

- GTP cap: the MT is stabilized by some GTP-bounded tubulin dimers at its growing end. This theory is supported by the fact that MT polymerization made using guanylyl-( $\alpha$ ,  $\beta$ )-methylene-diphosphonate (GMPCPP, a non-hydrolysable analogue of GTP) does not show this behavior [34] and that protofilaments made of GTP tubulin are straight while the GDP tubulin ones become curved [35,36];
- Lattice defects: they seem to be involved in MT dynamics [37] allowing dimer addition and removal [38];
- Microtubule Associated Proteins (MAPs): these are proteins that bind to MTs and affect their dynamics, either promoting dissociation and catastrophe or stabilizing them [39];
- Post-translational modifications: these are modifications in the tubulin structure that influence MT dynamics and are reviewed in [40];
- Environmental conditions: several studies showed that ionic concentration, pH, heavy water ( $D_2O$ ) and temperature affect MT polymerization [41-45].

The cell regulates MT dynamics and organization differentially in different cell regions and during different cellular activities and this complex process involves some of these effects on MTs (Figure 1.6).

MTs work alone or in small groups in the cell so they need important mechanical properties. In particular, they show a Young modulus of about 1 GPa, several

order of magnitude greater than the shear modulus, which does not exceed some MPa, making them a strongly anisotropic structures. Moreover, their persistence length is estimated to be about 1 mm, which means they are stiff and linearly organized structures. These properties origin from different reasons, one of which is the fact that their longitudinal bonds are stronger than the lateral ones, which is reviewed in [46,47].

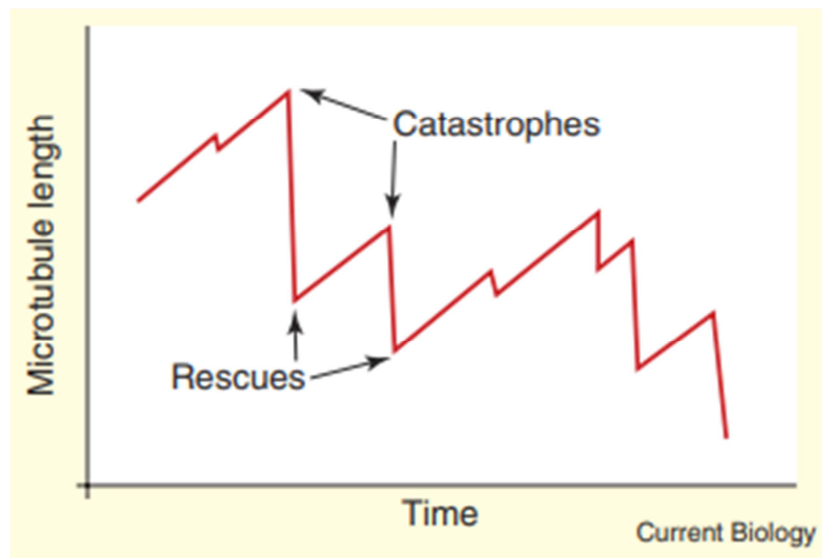


**Figure 1.5:** Dynamic instability during MT growth. Figure taken from Sept, D.; Microtubule Polymerization: One Step at a time. Current Biology, 2007, 17(17):R764-R766.

MTs have also very important electrostatic properties, reviewed in [48]: tubulin dimers have a bare charge of about  $-52e$  (from the 3RYF structure) which is present also at physiological pH [49] and almost a half of it is located on C-termini of both monomers. This charge, unusually high with respect to other proteins, gives rise to important phenomena including long-distance propagation of ionic signals, signal amplification and memristive behavior [50-53], all suggesting that MTs can act as signal transmission lines and memristive components in the cell, making them an interesting candidate for the development of nano devices in the future [48]. MTs' electrical properties depend also on the solution: since amino acids are zwitterions tubulin charge changes depending on the pH, so its value can vary on them. In addition,

according to numerical calculations ionic concentration plays a role in determining MT conductivity, which seems to be greater or lower than the buffer solution depending on a threshold of around 100 mM [54].

MTs electromechanical characteristics make them suitable to carry out a lot of functions in the cell:

- Compressional strength resistance of the cytoskeleton;
- Mitotic spindle during mitosis;
- Intracellular transport: “roads” for motor proteins like kinesin and dynein;
- Cell motility: cilia and flagella components;
- Signaling: mechanotransduction, which is the conversion of a mechanical stimulus in an electrical signal.

In addition to these functions, Penrose and Hameroff proposed MTs as the cellular structure for their Orchestrated–Objective Reduction (Orch–OR) theory of consciousness [55], which is a speculative theory based on quantum mechanics that requires experimental validation.

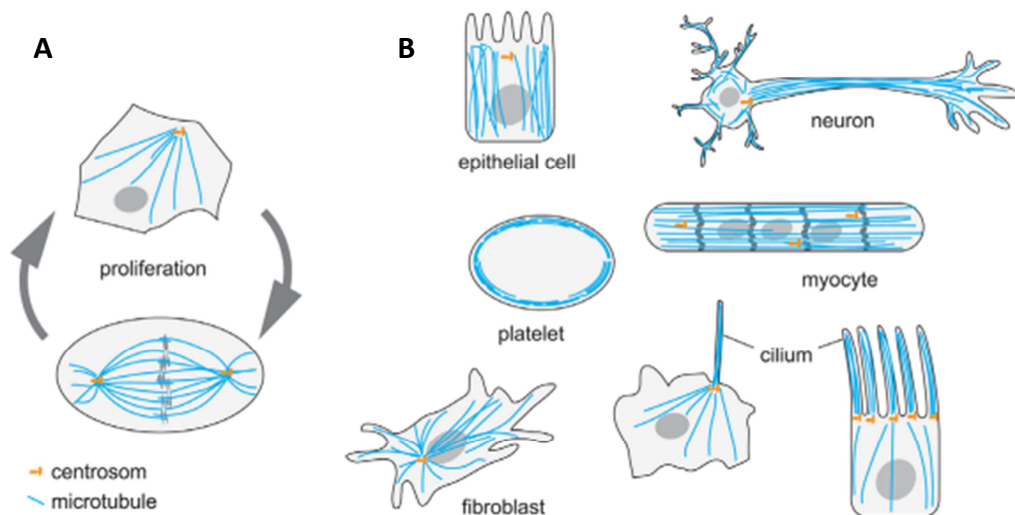


**Figure 1.6:** MTs organization in different cell phases (A) and cells (B). Picture taken from Matis, M. The Mechanical Role of Microtubules in Tissue Remodeling. *BioEssays*, 2020, 1900244.

Since MTs are involved in a lot of cellular functions, alterations of their activity are involved in several pathologies. In particular their mechanical role and their

contribution to mechanotransduction pathways of Reactive Oxygen Species (ROS) [56] can be linked with pathologies involving skeletal muscles such as Duchenne muscular dystrophy [57] and to heart failure [58]. In addition, altered MT activity is linked to neurodegenerative diseases such as Alzheimer's and Parkinson's diseases [59-61], with the former being correlated also to heart failure [62]. Finally, their role in mitosis makes them play a fundamental role in cancer cells because, as explained above, these cells replicate at a higher rate than healthy ones, so their MTs need to be adapted to this abnormal activity. As already stated above, cancer cell activity is a consequence of a genetic damage so maybe some altered gene expression can influence MT behavior. Moreover, tumor microenvironment is very different from the normal physiological one, so also the signaling activity would be different under different conditions like pH, ionic concentration and D<sub>2</sub>O's altered concentration and depletion. These effects change MT polymerization rates and are expected to play a role in MT and cancer dynamics. As an example, D<sub>2</sub>O alters the mitosis duration [63].

Because of their role in mitosis MTs became of great interest in chemotherapy research and a lot of drugs were found to be antimitotic agents binding to MTs [64-68]. Chemotherapy drugs can be classified into two groups according to their effects, namely:

- Destabilizing agents: they inhibit polymerization;
- Stabilizing agents: they stimulate polymerization.

It is important to underline that despite this classification based on high drug concentrations almost all drug effects at low concentrations result in the suppression of MT dynamics rather than a variation of the polymerized mass [64]. Antimitotic drugs bind to different tubulin domains and the most important sites are:

- Vinca domain: this domain can bind different drugs, among which the most studied is vinblastine. This domain is supposed to be located close to the GTP site and to the residues 177-215 of  $\beta$ -tubulin but from experimental results it appears that different binding site are also present [68-70];

- Colchicine site: this site binds colchicine, the first drug found, and its derivatives. Studies found that this site is located on  $\beta$ -tubulin, close to its interface with the  $\alpha$  subunit, explaining why this drug seems to interact with both monomers [68,71,72];
- Taxol site: it is the binding site for paclitaxel (taxol), its derivatives and other drugs. This site is located in the middle of the  $\beta$ -monomer, in the luminal side of the MT wall and in contact with the M loop [68].
- Other sites: there are drugs binding to tubulin whose binding sites are not yet determined and supposed to be different from the previous ones, like estramustine [73] and benzamidazoles [68].

The vinca domain and the colchicine site-binding drugs belong to the destabilizing agents group, while taxol site-binding drugs belong to the stabilizing agents group [67]. A summary of some of the most important antimitotic drugs is provided in Table 1.1. Interestingly, all sites are located on  $\beta$ -tubulin, suggesting that this monomer plays the most important role in MT dynamics. Proper understanding of MTs is therefore fundamental in the fight against cancer and with this project we hope to provide better information on the dynamics of these organelles.

**Table 1.1:** Some antimitotic drugs divided by their binding sites. Table adapted from ref. [64].

Binding domain	Related drugs or analogues	Therapeutic uses	
Vinca domain	Vinblastine (Velban)	Hodgkin's disease, testicular germ-cell cancer	
	Vincristine (Oncovin)	Leukaemia, lymphomas	
	Vinorelbine (Navelbine)	Solid tumours, lymphomas, lung cancer	
	Vinflunine	Bladder, non-small-cell lung cancer, breast cancer	
	Cryptophycin 52	Solid tumours	
	Halichondrins (such as E7389)	–	
	Dolastatins (such as TZT-1027)	Potential vascular-targeting agent	
	Hemiasterlins (such as HTI-286)	–	
	Colchicine domain	Colchicine	Non-neoplastic diseases (gout, familial Mediterranean fever)
		Combretastatins (AVE8062A, CA-1-P, CA-4-P, N-acetylcolchicinol-O-phosphate, ZD6126)	Potential vascular-targeting agent
2-Methoxyestradiol		–	
Methoxybenzene-sulphonamide (such as ABT-751, E7010)		Solid tumours	
Taxane site	Paclitaxel (Taxol), TL00139 and other analogues of paclitaxel	Ovarian, breast and lung tumours, Kaposi's sarcoma; trials with numerous other tumours	
	Docetaxel (Taxotere)	Prostate, brain and lung tumours	
	Epothilones (such as BMS-247550, epothilones B and D)	Paclitaxel-resistant tumours	
	Discodermolide	–	
Other microtubule binding sites	Estramustine	Prostate	

## 2 EXPERIMENTS

### 2.1 Experimental procedure

#### 2.1.1 Normal and cancerous prostate cells

Measurements on prostate cells (normal and cancerous) are done in order to study their characteristics and to determine if there are any differences between different cell lines. Three cell lines were investigated in this project:

- RWPE cells: epithelial cells derived from the peripheral zone of a histologically normal adult human prostate;
- LNCaP C4-2B cells: Lymph Node Carcinoma of the Prostate cell line, derived from human adenocarcinoma and with low metastatic potential;
- PC-3 cells: human prostate cancer cell line derived from bone metastasis of grade IV of prostate cancer, has high metastatic potential.

For the sample preparation cells are cultured in a petri dish, using Dulbecco's Modified Eagle Medium (DMEM) as culture medium. After culturing the sample, the old cellular media is removed from the petri dish and the sample is rinsed with Phosphate-Buffered Saline (PBS) solution (at 37° C). After gently rinsing the sample a couple of times, the PBS is removed. The glass coverslip is cleaned from the outside of the petri dish and a drop of refractive index matching oil is deposited on the previously etched region of the coverslip. Finally, fresh cellular media (DMEM, at 37° C) is added to the petri dish and the sample is placed in the incubator-like chamber, inside the enclosure of the phase contrast microscope. The sample is let to stabilize for ten minutes inside the chamber. The temperature is kept constant at 37° C throughout the entire experimental procedure.

Measurements are taken for 3 minutes and 20 positions are investigated in parallel (Multi Mode Fiber configuration, see section 2.2). These tests are useful to confirm that the platform can detect the differences between cell lines, in

particular their elasticity [74], whose variation can be used to evaluate the drugs' efficacies against the cells exposed to them [75].

### 2.1.2 Chinese Hamster Ovary (CHO) cells

To further investigate the platform's performance, measurements on Chinese Hamster Ovary (CHO) cells were performed. In this case only one cell line was used but different cell states were investigated, in order to see if the platform can detect differences between:

- Flat cells;
- Elongated cells;
- Round cells;
- Dividing cells;
- Cell monolayer.

Differences are expected to occur because the cell shape is mainly determined by the cytoskeleton, whose organization is fundamental in determining the cell's mechanical properties. If the platform is therefore capable of sensing the differences between cells it could be in principle used when the cell changes its state or undergoes apoptosis in response to drug treatments, especially when the drug acts on the cytoskeleton. As a consequence, it would be possible to evaluate the drug efficacy [75] using this platform.

The sample is prepared in a similar way as in the experiment with prostate cells and measurements are taken for 3 minutes, following 30 positions (MMF configuration, see section 2.2).

### 2.1.3 CHO cells treated with Nocodazole

Nocodazole, or Methyl [5-(2-thienylcarbonyl)-1H-benzimidazol-2-yl] carbamate (IUPAC name), is a drug used in chemotherapy because of its effects on MTs and its structure is shown in Figure 2.1. It is believed that this drug has two binding sites on tubulin with different affinity [76] and at least one of them overlaps with the colchicine binding site [77]. Nocodazole is a MT destabilizing agent whose

effects are strongly dependent on its concentration inside the cells, as is also the case with other drugs, which was explained in section 1.4. In particular:

- at high concentrations ( $> 1 \mu\text{M}$  in cells) it inhibits polymerization, which leads to MTs disruption [78-80];
- at low concentrations (4 nM-12  $\mu\text{M}$  in vitro, 4-400 nM in cells) it inhibits MT dynamics without changing the polymer mass [81,82].

Because of this behavior, experiments to explore both regimes were conducted on Chinese hamster ovarian epithelial (CHO) cells, for which MT disruption was observed after the administration of Nocodazole with a final concentration of 10  $\mu\text{M}$  in the sample [78].

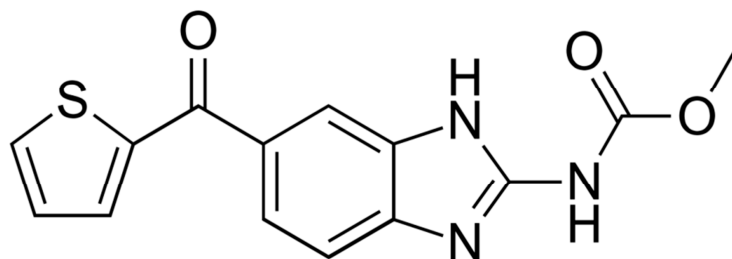


**Figure 2.1:** Nocodazole structure.

The sample preparation is done in the same way as for the previous experiments.

Three experiments on three different samples were performed:

- Experiment 1: high concentration regime which fully disrupts MTs, 1 drop of Nocodazole diluted in DMEM. The workflow is outlined the following:
  - Baseline measurements during the first 30 minutes;
  - 50  $\mu\text{L}$  of Nocodazole solution (in DMEM, 200  $\mu\text{M}$ ), is added to the sample for a final drug concentration of 10  $\mu\text{M}$  (in 1 mL of cellular media). A single drop is administrated. The buffer Nocodazole solution (5mg/mL) is diluted in DMEM instead of the more commonly used dimethyl sulfoxide (DMSO) because this allows assessing the effect of the Nocodazole alone with minimal influence of the DMSO

on both the change in reflectivity and the toxicity from the DMSO content.

- Experiment 2: high concentration regime, multiple drops of Nocodazole are diluted in DMEM. The workflow of the experiment is outlined in the following:
  - Baseline measurements during the first 60 minutes;
  - 50  $\mu\text{L}$  drops of Nocodazole solution (20  $\mu\text{M}$ ) are then administrated. Every drop corresponds to a final drug concentration of 1  $\mu\text{M}$  and 3 drops, 1 every 60 minutes, are administrated.
- Experiment 3: high concentration regime, single drop diluted in DMEM administrated. The workflow is outlined in the following:
  - Baseline measurements during the first 5 minutes;
  - 50  $\mu\text{L}$  of Nocodazole solution (in DMEM, 20  $\mu\text{M}$ ), is added to the sample for a final drug concentration of 500 nM (in 2 mL of cellular media). A single drop is administrated.

For every experiment, the signal detected using the setup described in the next section is analyzed as described in Chapter 3 in order to follow the system's evolution.

## 2.2 Experimental setup

To execute the experiments, an high-resolution photonic sensing platform was developed. The experimental platform must integrate the following functions:

- Light delivery;
- Detection capabilities;
- Cell culture incubator;
- Cytotoxic agents' delivery capability.

The integrated platform is schematically depicted in Figure 2.2 and a picture of it is shown in Figure 2.3. As can be seen, the investigated cells with their medium are placed in a petri dish. Under the dish, an optical waveguide is incorporated in order to perform coherence-gated Dynamic Light Scattering (DLS), whose

operating principles are explained in section 2.3, and the standard objective assembly is interchangeable. An interferometer was built around a standard multimode optical fiber (MMF) with core size of 62.5  $\mu\text{m}$  and fiber diameter of 125  $\mu\text{m}$ . Light from a super-luminescent diode centered at free-space wavelength  $\lambda_0 = 670 \text{ nm}$  with bandwidth  $\Delta\lambda = 40 \text{ nm}$  is launched into the fiber and then coupled into a 50/50 multimode splitter. The acquired signal is sent to a hardware Data Acquisition System (DAQ) that digitalizes it and from which the power spectrum is obtained. Once the power spectrum is obtained the analyses described in Chapter 3 are performed in order to follow the system's time evolution. In addition, the optical fiber system is incorporated into a standard microscope: this permits recording both dynamic signals and conventional microscopy images (typically phase contrast) collected in either a transmission or reflection mode. Around the microscope enclosure an incubator-like chamber was built in order to keep the cells in a controlled environment suitable for their survival. The fiber, which delivers and receives the signal, provides limited temporal coherence that limits the investigated volume depth to less than 20-30  $\mu\text{m}$ .

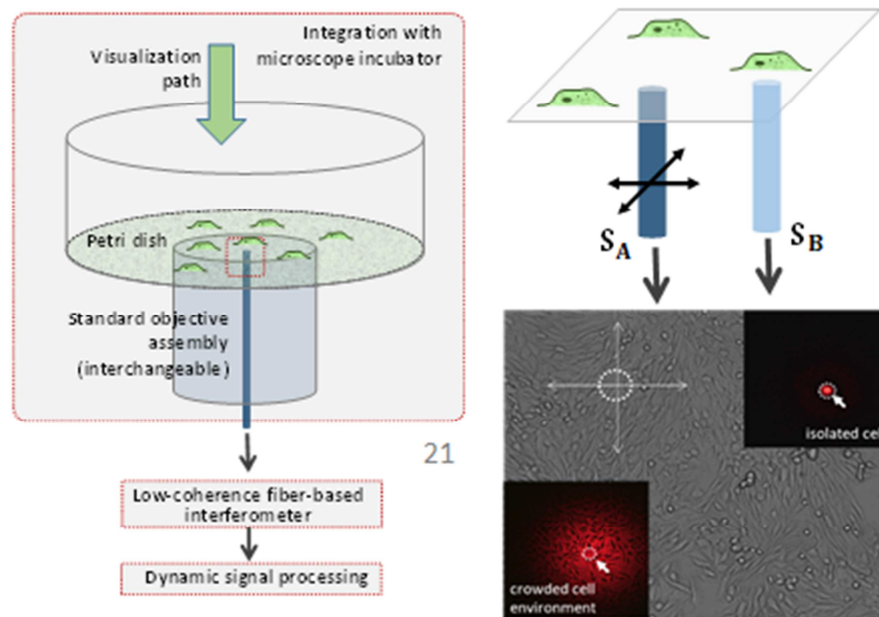


**Figure 2.2:** Schematic representation of the interrogation platform.

Experiments can be conducted in a single-mode fiber (SMF) configuration or in a MMF one. The SMF configuration allows a single location of coherent illumination, which is small with respect to the total sample volume: only a few microns can be viewed by it. Moreover, SMF provides the best optical signal, although it can be subjected to more noise. On the other end, the MMF configuration allows illumination of multiple spots, which is particularly useful in case of non-ergodic processes, and a better signal-to-noise ratio, but the optical signal has a low quality with respect to the SMF one and can introduce artifacts such as 2D arrays. In this configuration it is possible to investigate regions extended at most to hundreds of microns. Therefore, the configuration choice must be made carefully based on the investigated system. For experiments described in section 2.1.1 and 2.1.2 a MMF configuration is chosen while for experiments in section 2.1.3 a SMF configuration is used.

As first proof of capability of this system, a similar setup and an analogous analysis were used to continuously characterize the structural dynamics of hydrogels during their slow swelling process [83,84]. In particular, the information about both the morphology and the local viscoelastic properties of the hydrogel networks could be monitored over many tens of hours and results obtained indicate that there was clear correspondence between structural rearrangements within nanometer scale molecular assemblies and the parameters extracted with the data analysis. In addition, DLS works well with non-stationary dynamics in complex biological media, such as blood undergoing coagulation, as demonstrated in [85].

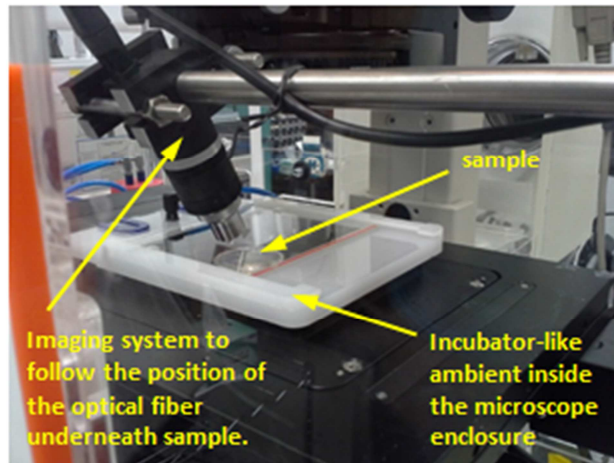


**Figure 2.3:** Picture of the experimental platform.

### **2.3 Coherence-gated DLS**

The platform implements a coherent-gated DLS. DLS is the measurement of scattering due to light-particle interactions as a function of time and was developed after the invention of the laser in 1960, which made coherent, collimated, stable and high-intensity light sources available for applications to chemistry, biology and physics [86,87]. DLS can be used in diverse set of configurations [87-90]:

- Self-beating: only the scattered light of the particles is detected;
- Homodyne: the signal is mixed with a non-frequency-shifted local oscillator before detection;
- Heterodyne: a mixture of the light scattered from particles and light reflected remotely or from ambient;
- Depolarized: the polarized and depolarized intensities are independently measured at different scattering angles;
- Mixed approach: combines more than one of the previous configurations and analyses.

The spatio-temporal coherent-gated DLS implemented in this platform can be seen as the (temporal) partially coherent interference of two (spatial) partially coherent speckle fields [91]. The two interfering fields are the stationary

reference field  $E_R(t)$ , corresponding to the reflection at the end facet of the optical fiber, and the time-varying back-scattered field  $E_S(t)$ , originated by the light scattering of the system under study. The configuration can be seen in Figure 2.4. The field fluctuations are determined by the fluctuations in the positions of various scattering centers within the volume interrogated. The contribution of the fluctuating component is on average weak with respect to the signal intensity due to the small sizes and relatively low refractive index contrasts that characterize typical biological systems so the DLS is performed under the heterodyne configuration at multiple independent locations, which provides the necessary amplification of the weak signal  $E_S$  [92-94]. As stated before, the investigated volume depth is at most 20-30  $\mu\text{m}$ , due to the limited temporal coherence, while the lateral resolution varies from few microns (SMF) to hundreds of microns (MMF). This configuration allows single scattering to dominate the measured signal, even in optically dense media [95-97].

During the coherence-gated DLS experiment the acquired signal is divided into blocks of typically 30-60 seconds for which the following parameters can be recorded [91]:

- Characteristic decorrelation time  $\tau$  of the scattering medium, which provides the information on the diffusing scattering centers;
- Time-averaged total power  $\langle I(t) \rangle$  or  $m^{(1)}$ , which is mainly due to the reference field and provides information on the Fresnel reflection;
- Total scattered energy of the intensity fluctuation  $\beta$ , which provides information on the dynamical properties of the scattering centers;
- DC value, which is the mean value of the signal and reflects the stationary component  $E_R$ .

Using these parameters, the statistical analysis described in section 3.1 can be performed using the acquired signal, from which the particle sizes and the system characteristics can be estimated.

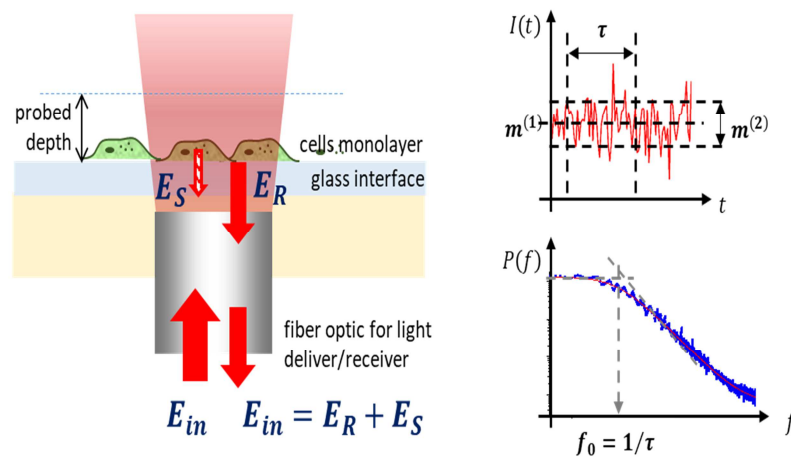


**Figure 2.4:** Coherence-gated dynamic light scattering implemented in this platform. The fiber receives scattered light from a selected region limited in both size and depth while the dielectric interface provides the reference field necessary for the heterodyne amplification. The fluctuating intensity constitutes the analyzed signal.

### 3 POWER SPECTRA ANALYSIS

#### 3.1 Theoretical remarks

The detected intensity signal can be described up to a constant factor as:

$$I(t) = |E_R + E_S(t)|^2 = |E_R|^2 + |E_S(t)|^2 + 2\text{Re}[E_R^* E_S(t)] \quad (3.1)$$

Since the fluctuating component  $E_S(t)$  has a zero mean value, the time-averaged signal intensity can be expressed as:

$$\langle I(t) \rangle = |E_R|^2 + \langle |E_S(t)|^2 \rangle = \langle I(t) \rangle + \delta I(t) \quad (3.2)$$

Because  $|E_R| \gg |\delta E_S(t)|$  (heterodyne configuration) the fluctuating part of the intensity becomes:

$$\delta I(t) \cong 2\text{Re}[E_R^* \delta E_S(t)] \quad (3.3)$$

To perform the statistical analysis one needs the intensity autocorrelation function (ACF)  $G_I(\tau) = \langle I(t)I(t + \tau) \rangle$  or, alternatively, its normalized value, which is expressed as:

$$g_I(\tau) = \frac{1}{N} + \frac{2I_R I_S}{N^2(I_R + I_S)^2} \text{Re}[g_E(\tau)] \quad (3.4)$$

One can then derive the procedure explained in ref. [85,91]. In eq. (3.4)  $I_R$  and  $I_S$  are the intensities of the reference and the scattered fields,  $N$  is the number of speckles, or coherent illumination locations, ( $N = 1$  for SMF) and  $g_E(\tau)$  is the normalized ACF of the electric field, which is described by the expression derived in [85,91]. From this relation it is possible to notice that the best optical signal is obtained in the SMF configuration because an increase in the number of spots  $N$  reduces the magnitude of  $g_I(\tau)$ .

The DLS measurement allows to measure  $g_E(\tau)$ , related to the decorrelation time  $\tau$ , and then to obtain the ACF of the fluctuation intensity. For practical reasons it is better to analyze the power spectrum  $P(f)$  of the normalized ACF of the intensity, that can be simply obtained by Fourier transforming  $g_I(\tau)$ . Given the power spectrum density (PSD) of the signal it is immediately possible to extract the following parameters:

- Total scattered energy of the intensity fluctuation  $\beta$ :

$$\beta = \int_0^{+\infty} P(f)df \quad (3.5)$$

Notice that this parameter is equivalent to the area of the PSD;

- Statistical moments of the i-th order  $m^{(i)}$ :

$$m^{(i)} = \int_0^{+\infty} P(f)f^i df \quad (3.6)$$

Notice that  $m^{(1)}$  corresponds to  $\langle I(t) \rangle$  and  $m^{(2)}$  is strongly related to  $\beta$ .

Then, since the single scattering is predominant, is possible to use standard micro rheology analysis. To do so, the first step is to decompose the normalized  $P(f)$  in a sum of discrete Lorentzian contributions:

$$\frac{P(f,t)}{\beta} = \frac{2}{\pi} \sum_{i=1}^N \frac{a_i(t)/\tau_i(t)}{f^2 + (1/\tau_i(t))^2} \quad (3.7)$$

With  $\sum_{i=1}^N a_i(t) = 1$ . In eq. (3.7)  $a_i(t)$  are the relative amplitudes and  $\tau_i(t)$  are the relaxation times of the i-th Lorentzian [98,99]. Then, by multiplying the relative amplitude at a certain time  $t$  times the corresponding  $\beta$  value, it is possible to obtain the absolute amplitude  $A$  of the Lorentzian. At this point the scattering particle size distribution can be obtained by solving for the hydrodynamic diameter  $d_h$  using the following relation, derived from the Stokes-Einstein relation [86]:

$$f_c = \frac{1}{\tau} = \frac{q^2 k_B T}{6\pi^2 d_h \nu} \quad (3.8)$$

where  $f_c$  is the corner frequency,  $k_B = 1.38 \cdot 10^{-23}$  J/K is the Boltzmann constant,  $T$  is the absolute temperature,  $\nu$  is the viscosity of the suspending medium  $q = 4\pi n \sin(\vartheta/2)/\lambda_0$  is the magnitude of the scattering vector, with refractive index  $n = 1.331$ , scattering angle  $\vartheta = \pi$  (back-scattering configuration) and free space wavelength of the fiber is  $\lambda_0 = 670$  nm.

Moreover, the spectral decomposition can be used to calculate the mean squared displacement (MSD) of the scattering particles [86]:

$$\langle \Delta r^2(t) \rangle = -\frac{6}{q^2} \ln \left[ \sum_{i=1}^N a_i \exp\left(-\frac{2\pi t}{\tau_i}\right) \right] \quad (3.9)$$

where  $r$  is the displacement of the scattering centers. The MSD can be used to estimate the local viscoelastic properties of the suspending medium such as the

complex viscoelastic modulus  $G^*(\omega)$  [100,101], for which the following expression can be derived:

$$|G^*(\omega)| \approx \frac{k_B T}{\pi a \langle \Delta r^2(1/\omega) \rangle \Gamma[1+\alpha(\omega)]} \quad (3.10)$$

Here,  $a$  is the particle radius,  $\Gamma$  indicates the gamma function and  $\alpha$  is the logarithmic slope of the MSD curve:

$$\alpha(\omega) = \frac{\partial \ln \langle \Delta r^2(t) \rangle}{\partial \ln(t)} \quad (3.11)$$

calculated at  $t = 1/\omega$ . From here the elastic component  $G'(\omega)$  and the viscoelastic one  $G''(\omega)$  of the viscoelastic modulus can be easily calculated as:

$$G'(\omega) = |G^*(\omega)| \cos(\pi\alpha(\omega)/2) \quad (3.12)$$

$$G''(\omega) = |G^*(\omega)| \sin(\pi\alpha(\omega)/2) \quad (3.13)$$

It is important to underline that the viscoelasticity calculated here is a local parameter so it must not be interpreted as a macroscopic rheological property because of the structural discontinuity around the scattering particles, which could also be hydrodynamically coupled with the surrounding medium [102,103]. The ratio of the viscoelastic components defines the frequency-dependent loss of tangent:

$$\gamma(\omega) = \frac{G''(\omega)}{G'(\omega)} \quad (3.14)$$

whose frequency-averaged value:

$$\bar{\gamma} = \left\langle \frac{G''(\omega)}{G'(\omega)} \right\rangle_{\omega} \quad (3.15)$$

can be followed over time to investigate the local material fluidity [100]: the greater its value, the softer the material is.

## 3.2 Procedure

The recorded signal is split and integrated every 30-60 seconds in order to study the power spectra and the parameters' evolution. The PSD values of every signal block for frequency range 1 Hz-10 kHz, with a 1 Hz resolution, and the DC values are processed using Matlab software.

From raw PSDs data, the averaged background noise (if recorded) is subtracted. After this outlier are removed using the Hampel identification criterion, the same procedure is applied to the power spectra with contrast less than 2 decades.

For every PSD the  $\beta$  parameter and the first and second moments  $m^{(1)}$  and  $m^{(2)}$  are calculated according to eq. (3.5) and (3.6) for the following frequency ranges:

- 1 Hz-10 kHz (entire spectrum);
- 1 Hz-1 kHz (low frequencies range);
- 100 Hz-1 kHz (medium frequencies range);
- 1-10 kHz (high frequencies range).

After this, the normalized power spectra are fitted according to eq. (3.7) with 2-4 Lorentzians (the number of Lorentzians is kept constant for the whole experiment). Using the fitting results the MSD, the viscoelastic modulus and its components, the loss of tangent and the hydrodynamic sizes are calculated according to eq. (3.8-3.14) in order to follow their evolution over time.

In order to improve the estimations and better identify the trends, the presence of outliers in the relaxation times and in the relative amplitude of the series are identified based on the moving median criterion with a window of ten values. When an outlier is found, the corresponding PSD is substituted with the related moving median PSD calculated over a window of ten blocks and the fitting procedure is performed again. Finally, the frequency-averaged loss of tangent is calculated according to eq. (3.15). Data are also processed in order to eliminate noise generated by the perturbations due to the drug administration. Since the probe can reach a depth of 20-30  $\mu\text{m}$ , the investigation volume will move across the cell and also include the surrounding medium.

## 4 POWER SPECTRA RESULTS

### 4.1 Prostate cells

In the experiment with prostate cells, three cell lines were monitored in order to investigate their properties. Details of the experimental procedure are explained in section 2.1.1 and images of the cells are shown in Figure 4.1.

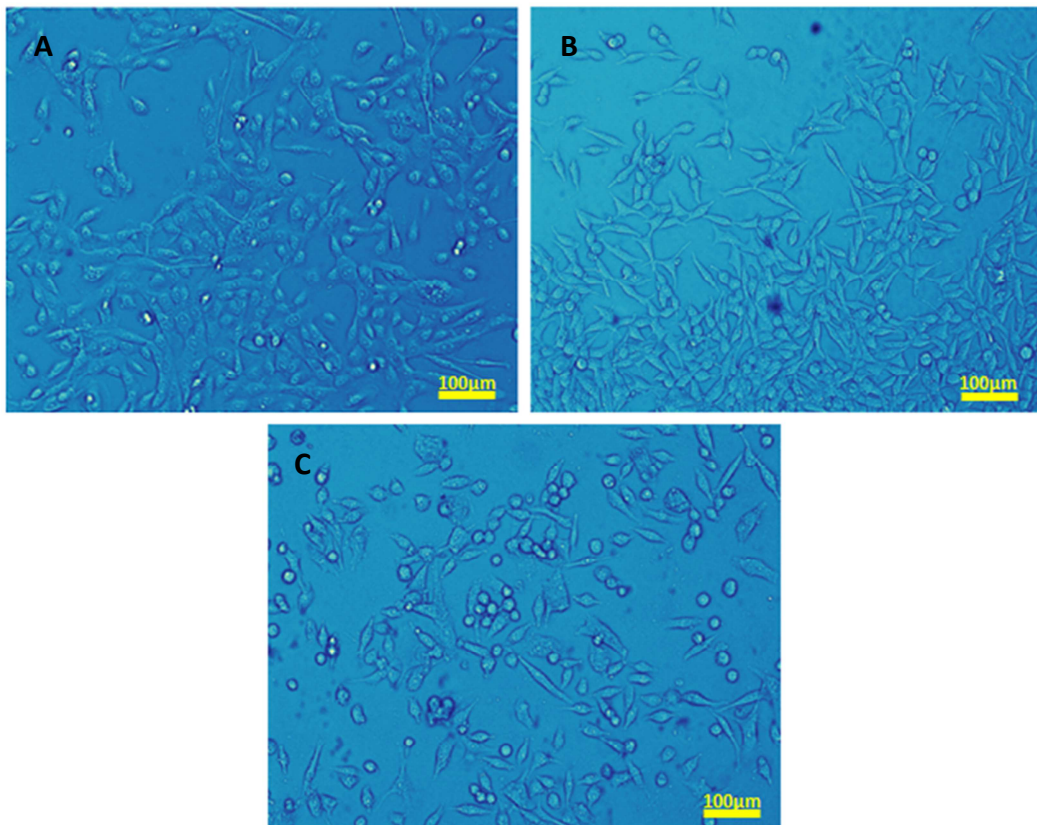


**Figure 4.1:** (A) RWPE prostate cells. (B) C4-2B cancer cells. (C) PC-3 cancer cells

Based on the analysis over 20 samples, the time-averaged loss of tangent is obtained for every cell line and results are shown in Figure 4.2. The time-averaged loss of tangent is a quantity related to the material's local softness and in particular the high frequency range around 1 kHz gives information on the diffusion over short timescales [85]. Because of this, comparing its value in this

frequency range gives information on the relative elasticity between the different cell lines: the higher the loss of tangent, the softer the material. From Figure 4.2 it is therefore possible to conclude that normal cells are the stiffest while cancer cells are softer, with the C4-2B line (the less aggressive) softer than the PC-3 one (the most aggressive). In addition, the two cancer cells curves have similar shape with a plateau in the hundreds of Hertz region while normal cells do not have it. This is in agreement with results found in Ref. [74] using AFM technology, although differences in the viscoelastic moduli found with our photonic platform (table 4.1) are less important in magnitude than the differences in elastic moduli measured in the cited paper. This can be explained by the fact that this photonic platform sees only a local value and not a global one. In addition, similar changes in cells elasticity have been found in breast cell lines [104].

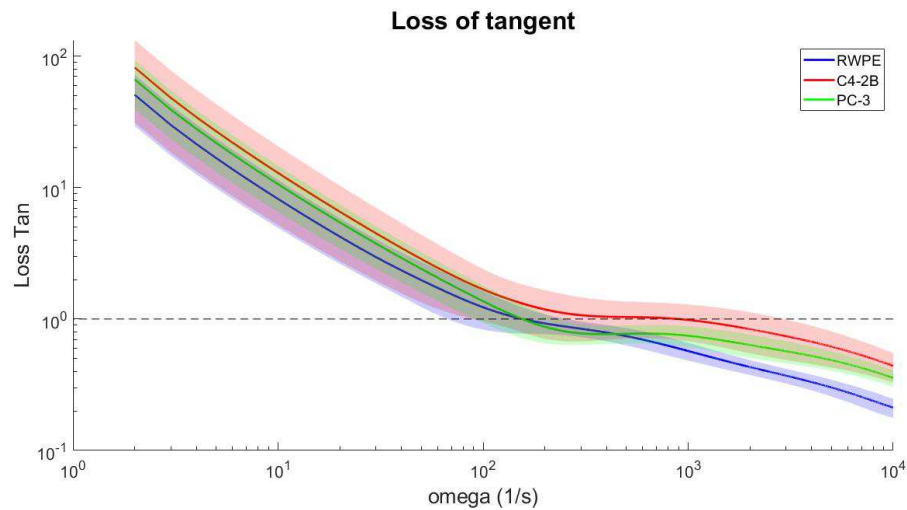


**Figure 4.2:** Time-averaged loss of tangent of the three cell lines. The line represents the mean value over the investigated positions while the shaded plot represents the standard deviation.

A t-test on the results shown in Table 4.1 is performed to see if the differences found are statistically significant. The test done is a heteroscedastic two-tails test because there are two samples with different variances for every test (although for the couple RWPE/C4-2B variances are similar) and is performed using the Microsoft Excel software.

**Table 4.1:** Viscoelastic moduli at 1 kHz of the prostate cell lines with their standard deviations.

<b>Cell line</b>	<b>Viscoelastic modulus [N/m<sup>2</sup>]</b>
RWPE	130.27 ± 31.60
C4-2B	184.07 ± 30.07
PC-3	170.01 ± 57.11

Table 4.2 shows results of the statistical analysis. As can be seen, RWPE cells (normal ones) are statistically different from both the cancer cell populations because the p-value is less than 0.05 in both cases, while the two cancerous cell lines do not show statistically significant differences ( $p > 0.05$ ). The platform is therefore at least capable to distinguish between normal and cancerous cells by measuring their elasticities.

**Table 4.2:** p-values for all the cell pairs.

<b>Pair</b>	<b>p-value</b>
RWPE - C4-2B	2.64e-06
RWPE - PC-3	0.01
C4-2B - PC-3	0.34

## **4.2 CHO cells monitoring**

In the CHO cells monitoring experiment flat, elongated, round, dividing cells and cells monolayers were monitored. In addition, data from the background were recorded to estimate the noise. A more detailed description is already provided in section 2.1.2 and images of the cells are shown in Figure 4.3.

From the PSD analysis, the loss of tangent is obtained for every cell state and results are shown in Figure 4.4. From this figure, it is possible to see that the dividing cells are the softer ones, then flat and round cells have an intermediate and similar stiffness and elongated cells and the monolayer are stiffest.

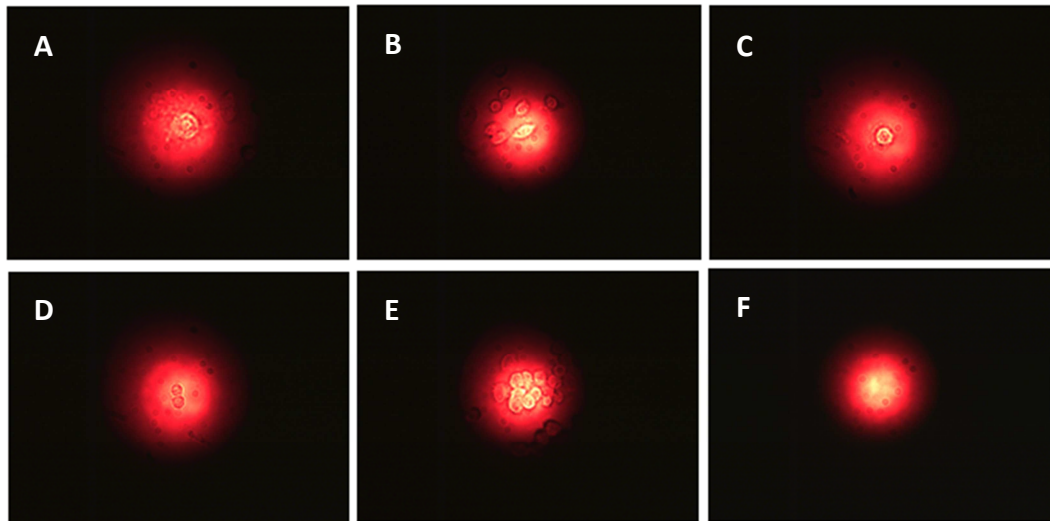


**Figure 4.3:** (A) Flat CHO cell. (B) Elongated CHO cell. (C) Round CHO cell. (D) Dividing CHO cell. (E) CHO cells monolayer. (F) Background.

Table 4.3 shows the viscoelastic moduli at 1 kHz with the corresponding standard deviations. Results are in agreement with the loss of tangent except for the round cells but this can be due to the high standard deviation, which means that there is a lot of variation in this cell state.

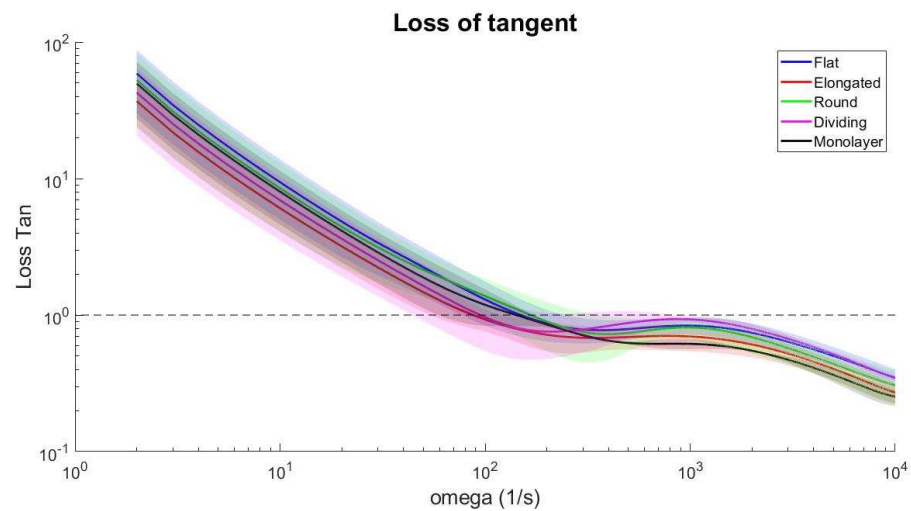


**Figure 4.4:** Frequency-averaged loss of tangent for flat (blue), elongated (red), round (green), dividing (magenta) CHO cells and for the CHO cells monolayer (black). The solid line is the averaged value over the investigated positions and the shaded plots represent the standard deviations.

**Table 4.3:** Viscoelastic moduli at 1 kHz for the different cell states with their standard deviations

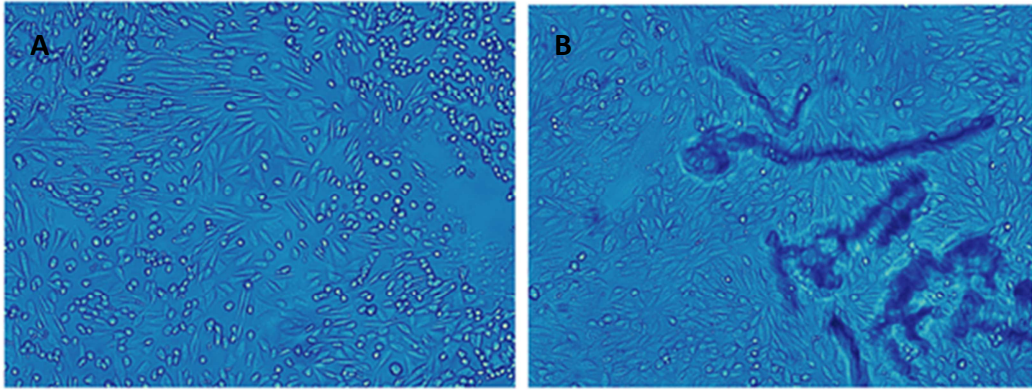
<b>Cell state</b>	<b>Viscoelastic modulus [N/m<sup>2</sup>]</b>
Flat	131.01 ± 42.68
Elongated	104.08 ± 24.26
Round	166.90 ± 101.54
Dividing	125.43 ± 59.44
Monolayer	97.57 ± 14.63

The platform seems capable of determining differences between different cells states in the same cell line. This means that if the cell changes its state during the measurement we could in principle detect it. This is again possible because the cell shape strongly depends on the cytoskeleton's organization, which determines also the cell's elasticity. The platform could be therefore capable of seeing changes in cell structure if they happen during the measurement process. This means that if drugs acting on MTs modify the cell's elasticity (and they are expected to do so because of MTs mechanical role) the platform could detect when this happens and so it can be used to estimate the drug's efficacy. No t-test is performed because there are only few data for some cell types.

### **4.3 CHO cells with Nocodazole**

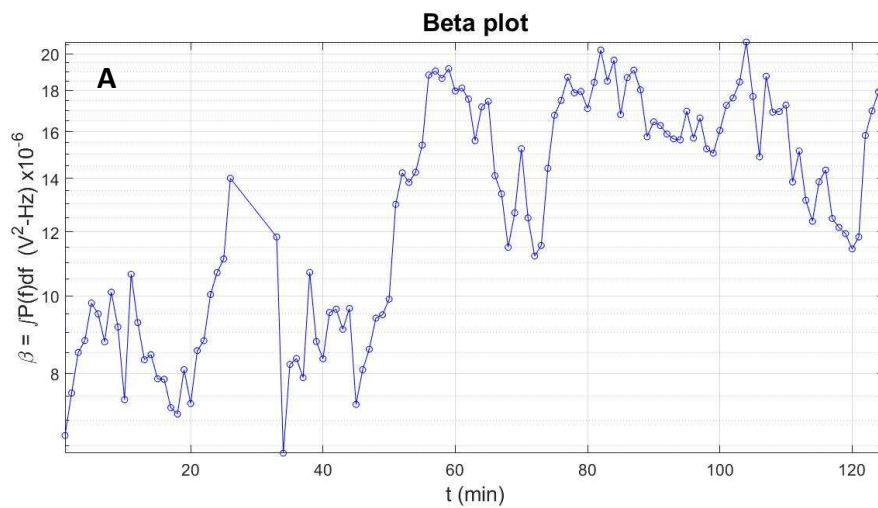
#### *4.1.1 Experiment 1*

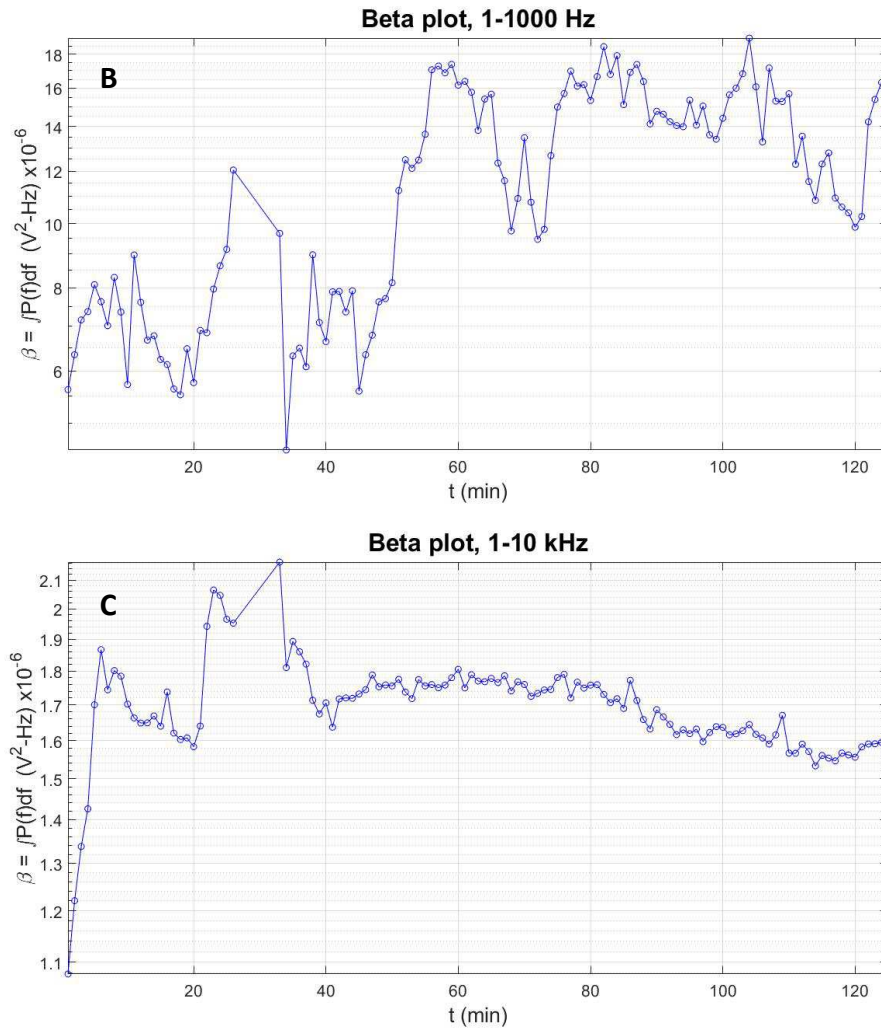
In experiment 2 a single drop of Nocodazole diluted in DMEM was administrated after 30 minutes for a final concentration of 10 µM in the sample to result in MT disruption. The measurement was taken in the SMF configuration. A more detailed description is provided in section 2.1.3 and images taken during the experiment are shown in Figure 4.5.



**Figure 4.5:** (A) CHO cells during baseline measurements (first 30 minutes). (B): CHO cells after Nocodazole effect, picture taken 90 minutes after the drug administration.

The beta plot for all frequencies and for the 1 Hz-1 kHz and 1-10 kHz bands are shown in Figure 4.6. From the beta plot it is possible to see that after about 50 minutes from the beginning of the experiment, so 20 minutes after the drug administration, the overall scattering activity (all frequencies, Figure 4.6.A) increases. The increase is due to the lower frequencies associated with larger structures in the cell, while the higher ones show a constant trend, as can be seen from Figures 4.6.B and 4.6.C.

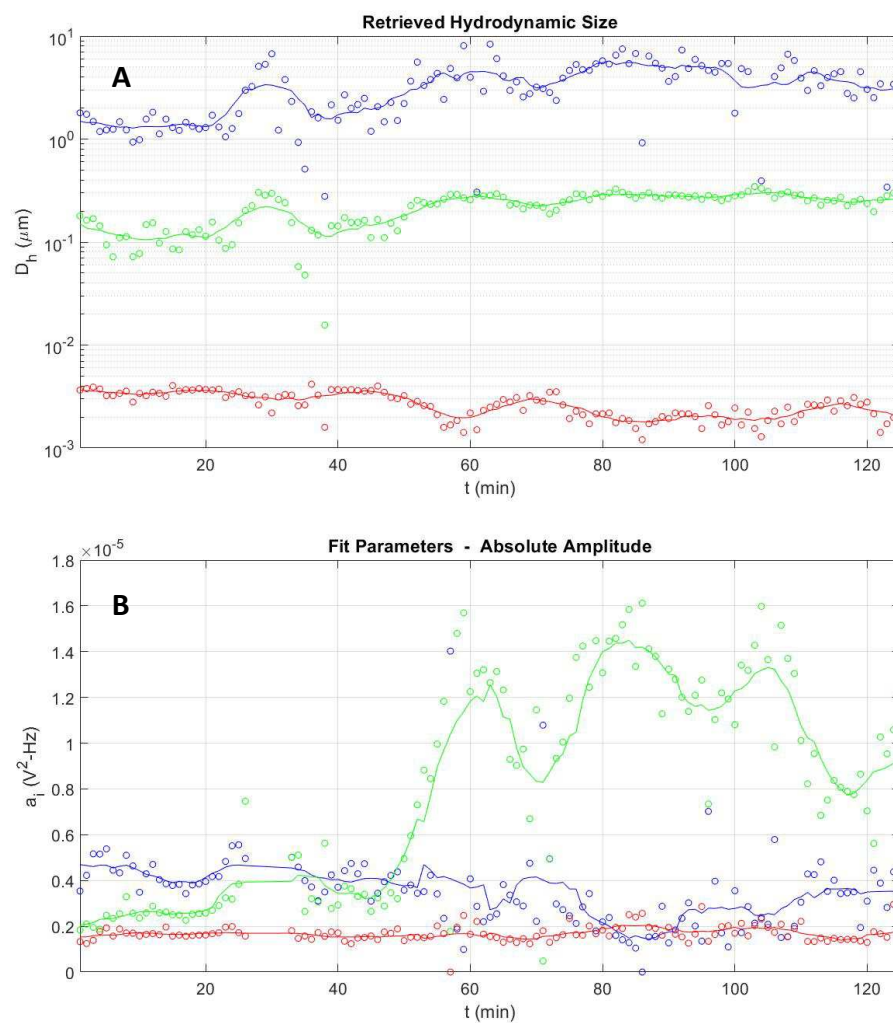




**Figure 4.6:** (A) Beta plot, all frequencies. (B) Beta plot, low frequencies: 1 Hz-1 kHz. (C) Beta plot, high frequencies: 1-10 kHz.

The power spectra were fitted using three Lorentzians and the associated amplitudes and hydrodynamic sizes are shown in Figure 4.7. The Figure shows a size distribution that does not change a lot during the experiment. The reason is that with the Lorentzians it is possible to see only three contributions while in cells there are a lot of compounds and organelles, so these can be thought of as divided in three classes that have an almost constant average size. In particular, it is possible to distinguish between micrometer-, hundreds of nanometers- and nanometer-scale components and it is important to underline that the DLS system implemented here can distinguish sizes differing from at least one decade. Regarding the amplitudes, while the smallest size contribution remains

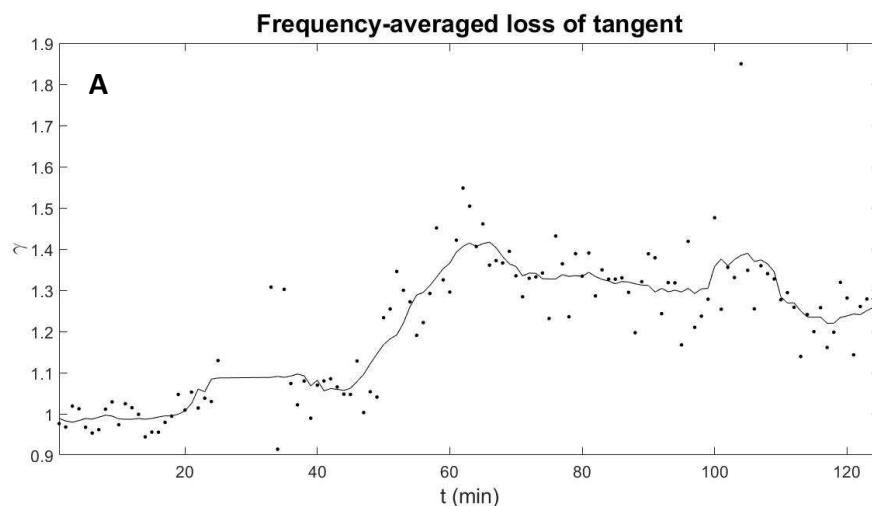
almost constant the other two change during the experiment: the microscale component shows a slightly decreased activity over time and the second-largest component increases its activity after about 50 minutes from the beginning of the experiment, in correspondence to the beta increment. These can be interpreted as proofs of the MT disruption in smaller structures such as oligomers and tubulin dimers and the consequent cell death. In both graphs the lines represent the moving averages over 10 values.

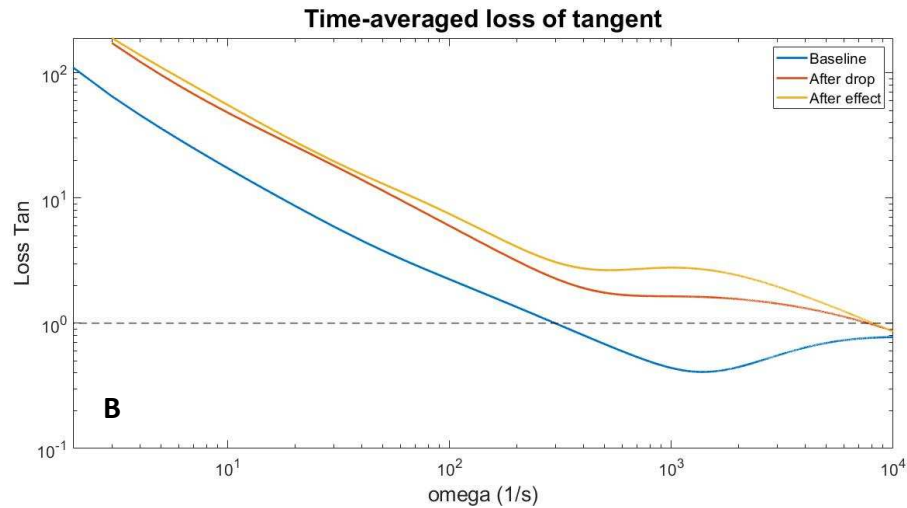


**Figure 4.7:** (A) Hydrodynamic sizes extracted from the fitting Lorentzians. (B) Absolute amplitudes of the Lorentzians. The amplitude colors refer to the size ones.

The frequency-averaged and the time-averaged loss of tangent plots are shown in Figure 4.8. The frequency-averaged loss of tangent can be seen as a measure

of the local material softness and is evident that after about 50 minutes there is an increase of its value. This can be interpreted as a transition to a softer material and to a more diffusive-like activity. These facts are again consistent with the MTs disruption since MTs are responsible for the mechanical properties of the cell and due to their dimensions they can be an obstacle to free 3D diffusion. The time-averaged loss of tangent, as described above, is another quantity that shows local stiffness. The plot of Figure 4.8.B shows an increase of the loss of tangent at 1 kHz when passing from the baseline (min. 1-26), to the transition phase after the drug administration (min. 40-60) and finally to the end of the experiment, after the drug has taken an effect (min. 90-125). This can be again interpreted as a transition from a stiffer to a softer state, which is consistent with the MT disruption expected from this experiment. Again, in the graph of Figure 4.8.A the line represents the moving average over 10 values. The interpretations of this first experiment with Nocodazole are supported by the fact that MTs contribute to the generation of the cell's nanoscale vibrations and Nocodazole treatment changes these vibrations characteristics [105] and also by the fact that cell softening was observed independently after treatment with Taxol [106].

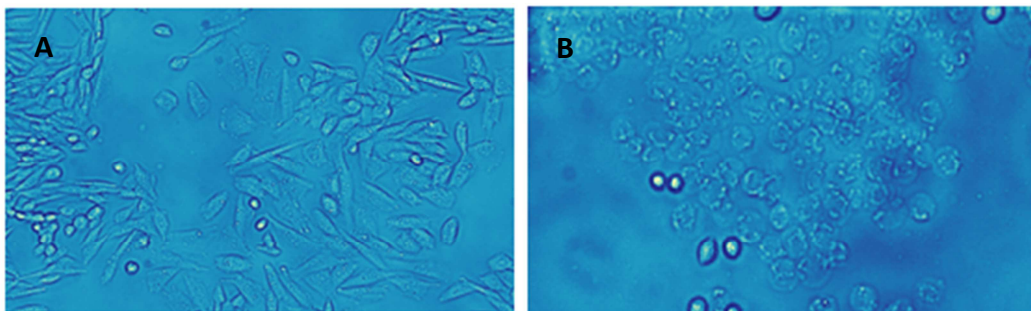




**Figure 4.8:** (A) Frequency-averaged loss of tangent. (B) Time-averaged loss of tangents during baseline measurements (blue line), after the drug administration (red) and during the last part of the experiment (yellow).

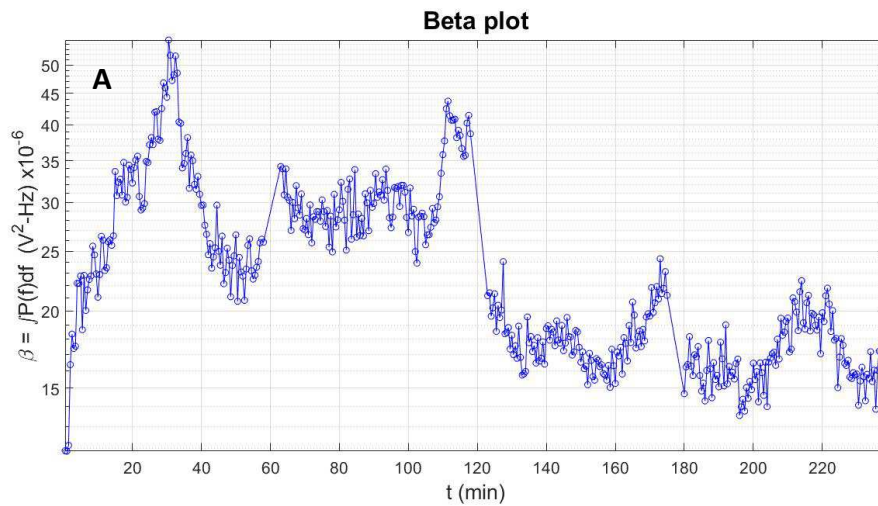
#### 4.1.2 Experiment 2

In experiment 2 the high concentration regime, from 1 to 3  $\mu\text{M}$ , was explored. Three drops were administrated and disruption of MTs was expected to happen. A more detailed description is provided in section 2.1.3. The fiber was in the SMF configuration and images before and after the treatment are shown in Figure 4.9. From the cell images it is possible to see an overall transition from a flat state to a round one, which indicates that cells have been poisoned by Nocodazole because when a cell is healthy it sticks to the substrate and becomes flat (via adhesion and spreading processes) while if it is not in a suitable environment it assumes a more rounded shape.



**Figure 4.9:** (A) CHO cells during baseline measurements (first 60 minutes). (B): CHO cells after Nocodazole effect, picture taken at the end of observation (240 minutes).

Figure 4.10 shows the beta plot for all, low and high frequency ranges, divided in the same way as before. It is possible to see in all plots a diminished beta value after the second drop, but this can be due to a change in the properties of the system since the fiber penetrates across the cell and feels also its surrounding. Moreover, in case of drug effects, this seems instantaneous, which is clearly impossible. Another possibility is that for the investigated cell the drug administrated before started acting while the second drop was administrated, meaning that the seen effect is due to the previous drop instead of the second one. Again, as in experiment 3, the variation is mainly due to a change in the low frequency range activity, but this time the behavior is opposite because there is a reduction in the system's activity. This could be related to the different drug administration regime. Since Nocodazole effects are strongly concentration-dependent, although a high regime is expected, maybe this particular cell is experiencing a low concentration regime.



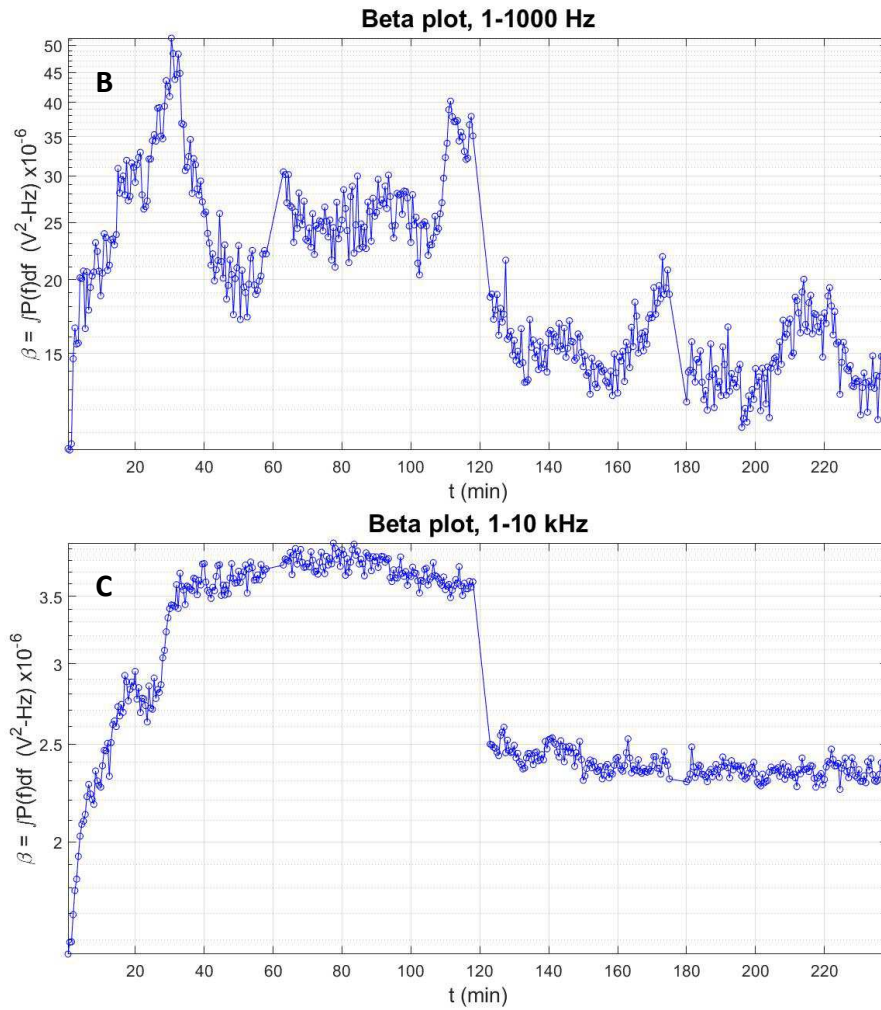


**Figure 4.10:** (A) Beta plot, all frequencies. (B) Beta plot, low frequencies: 1-1000 Hz. (C) Beta plot, high frequencies: 1-10 kHz.

Figure 4.11 shows the fitting results for the hydrodynamic sizes and the Lorentzians amplitudes. The fitting is done with three Lorentzians. The hydrodynamic sizes show the presence of a micrometer-, tens of nanometers- and a nanometer- scale components, whose sizes oscillate but do not show any important increment or decrement during the experiment. On the other hand, while the amplitudes of the smallest components remain almost constant, one of the biggest changes a lot during the experiment. The peak during baseline measurements can be due to cellular activity. Perhaps the cell is simply undergoing some changes in response to the environment or is passing through a different phase of the cell cycle. The most evident trend is the overall

diminished activity after the second drop, that is coupled with the presence of two peaks, smaller than the previous ones. This could be due to a change in the MT activity but for a more complete understanding it is better to look also at the loss of tangent.

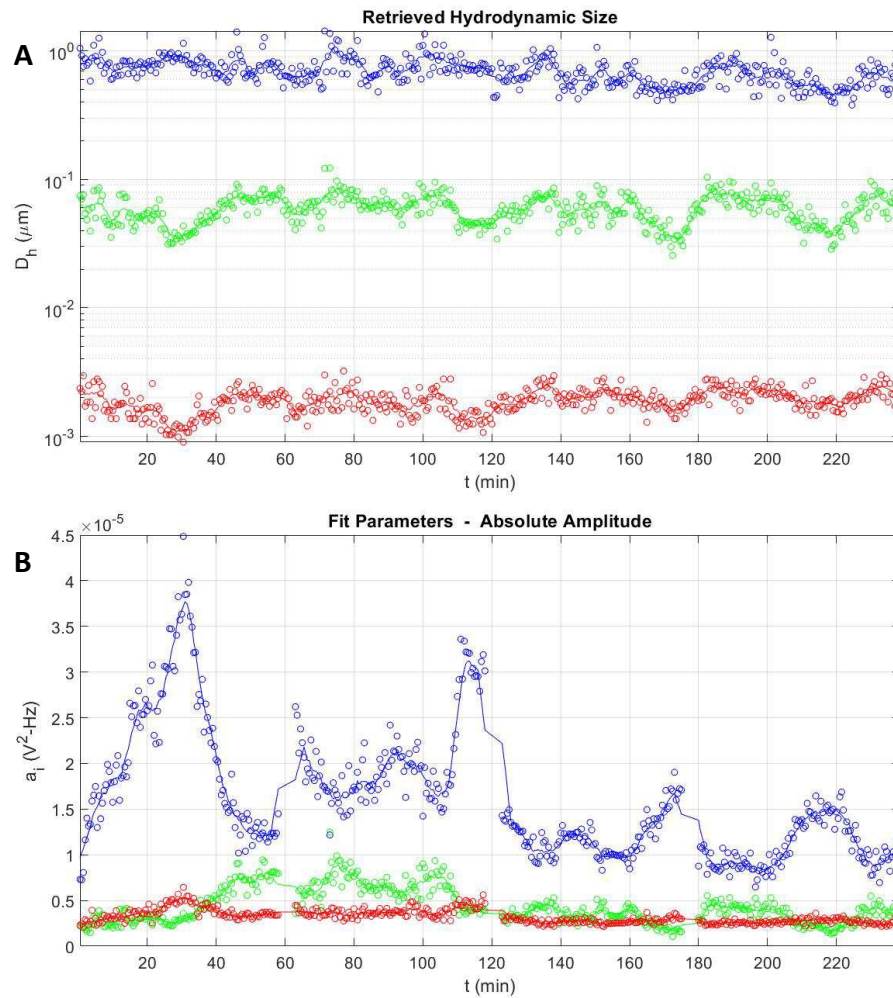


**Figure 4.11:** (A) Hydrodynamic sizes extracted from the fitting Lorentzians. (B) Absolute amplitudes of the Lorentzians. The amplitude colors refer to the size ones.

The frequency-averaged loss of tangent is shown in Figure 4.12.A. It can be seen that its average value is not changing a lot although there are several oscillations, meaning that the local rigidity of the system is not changing significantly. The time averaged loss of tangent at 1 kHz also does not show a large variation but it is possible to see that after the first drop, the structure becomes stiffer than the

baseline while the administration of the other drops increases the softness. A possible interpretation could be that after 1 drop MTs dynamics is inhibited and the cytoskeleton becomes stiffer while after the other drops MTs start disrupting. However, since the structure is not softer than at the beginning, the process is not complete and the cell is still alive. Moreover, Nocodazole effect is reversible [66] so this fact could play a role in fractionated administration experiments.

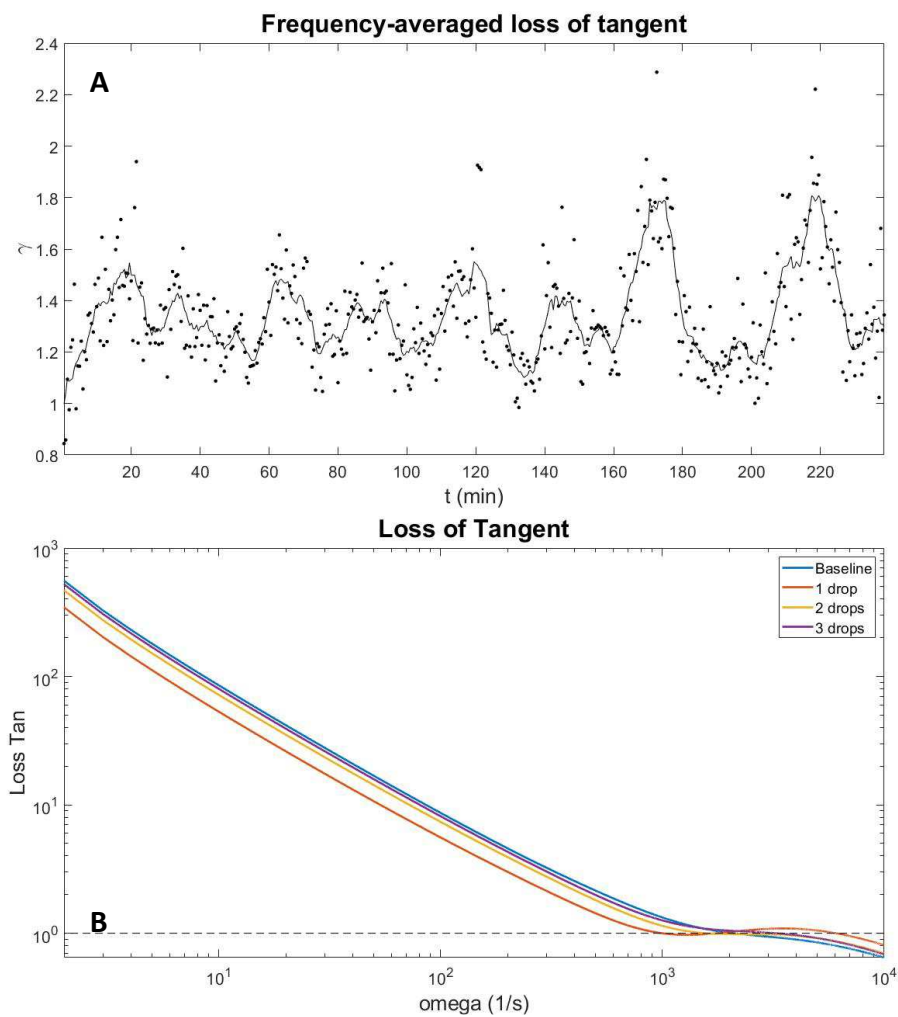


**Figure 4.12:** (A) Frequency-averaged loss of tangent. (B) Time-averaged loss of tangents during baseline measurements (blue line), after 1 drop (red), 2 drops (yellow) and 3 drops (violet).

### 4.1.3 Experiment 3

In experiment 3 a single drop of Nocodazole, for a final concentration of 500 nM, was administrated after 5 minutes in order to perform a high concentration experiment in which full disruption of MTs is expected (see section 2.1.3 for more details). The measurement was performed using the MMF configuration although only one position was investigated for all the experiment and images of the cells are shown in Figure 4.13. In this case, cells undergo again a shape transition from flat to round so the environment is not good for them and they are unhealthy or probably dead.

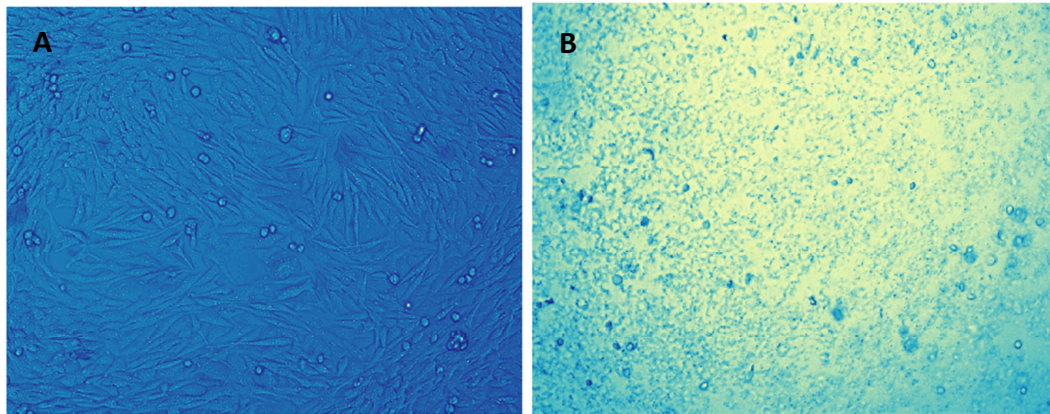


**Figure 4.13:** (A) CHO cells during baseline measurements (first 5 minutes). (B): CHO cells after Nocodazole effect, picture taken after 2 hours.

The beta plots are shown in Figure 4.14. From them is possible to see that after about 40 minutes (corresponding to 35 minutes after the treatment) the beta value increases for all frequency ranges, meaning that there is more scattering activity and the system's state is different. The increase in the activity is consistent with what was observed for experiment 1, so the effect on cells is similar, although now the transition is slower. In particular, in experiment 1 the transition happens in about 20 minutes (Figures 4.6-4.8), while now it happens in about 60 minutes. This can be due to the different drug concentration: before there was more drug so a faster effect is expected because the bigger number of interacting molecules.

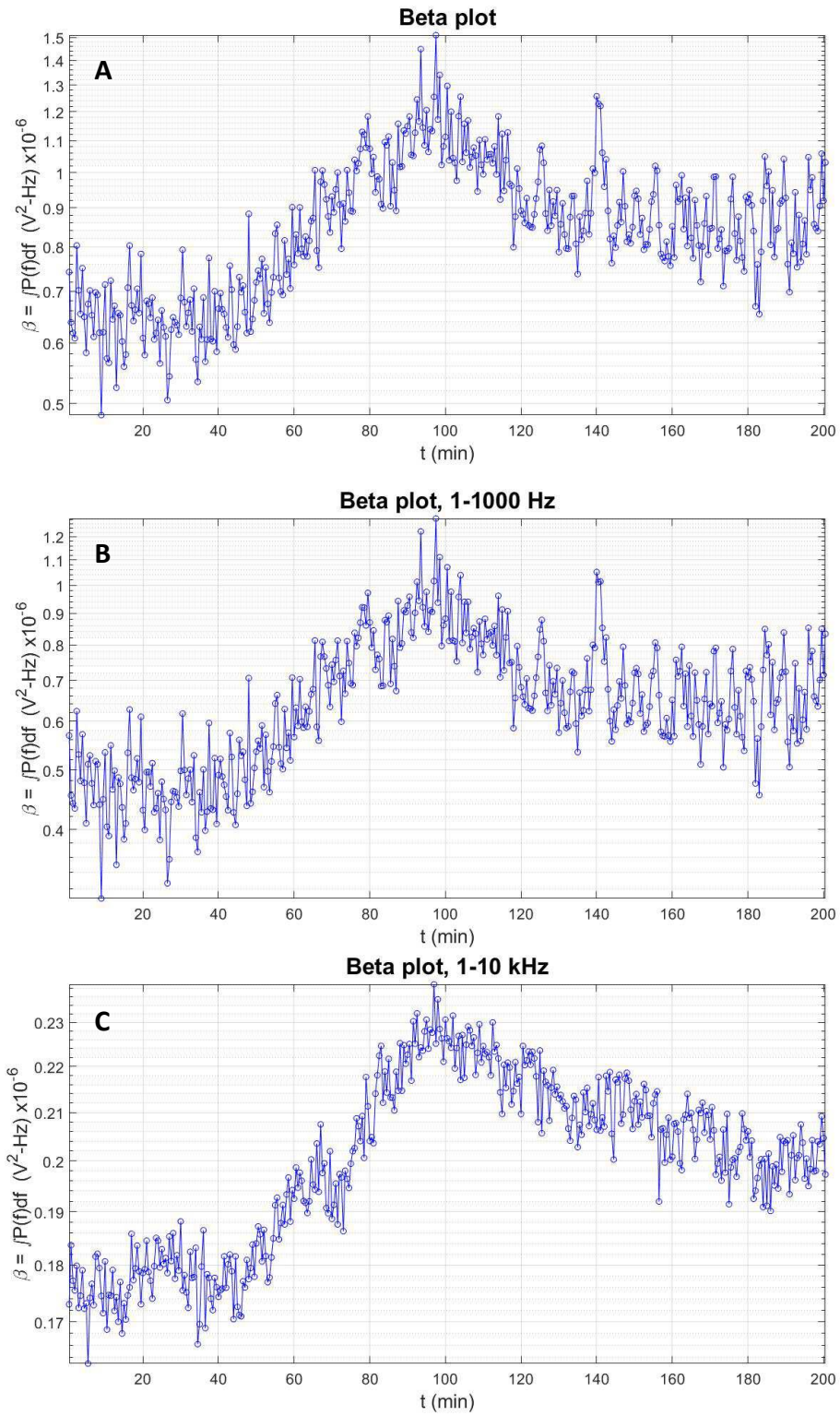


**Figure 4.14:** (A) Beta plot, all frequencies. (B) Beta plot, low frequencies: 1-1000 Hz. (C) Beta plot, high frequencies: 1-10 kHz.

The fitting procedure is performed with 3 Lorentzian functions and the results are shown in Figure 4.15. The cellular components are divided in two classes, one of micrometer-hundreds of nanometers scale, the other of nanometers scale, and both as in the other experiment do not change significantly. Regarding the amplitudes, while the smallest component activity remains constant, the higher one increases after about 40 minutes and then stabilizes at an intermediate value: this explains the beta variation. This result, coupled with the loss of tangent (Figure 4.16), can be interpreted as a proof of MT disruption.

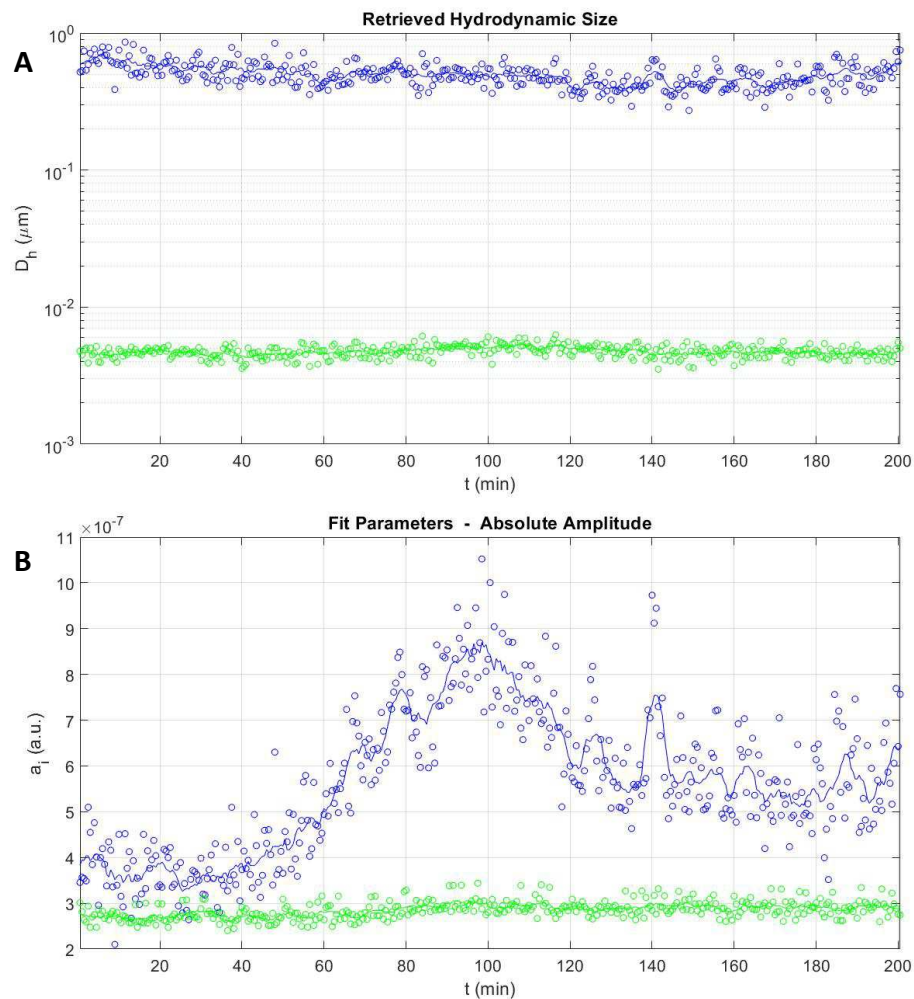


**Figure 4.15:** (A) Hydrodynamic sizes extracted from the fitting Lorentzians. (B) Absolute amplitudes of the Lorentzians. The amplitude colors refer to the size ones.

The frequency-averaged loss of tangent, shown in Figure 4.16.A, exhibits a behavior that strongly reflects the beta and the absolute amplitude of the Lorentzian variations. The material becomes softer after the drug administration and this is consistent with the MTs disruption, although the stiffness increases somewhat after reaching the peak. The time-averaged loss of tangent (Figure 4.16.B) confirms the anticipated changes in the material local properties because it shows a transition to a softer state after the drug administration and a final but low stiffening of the material.

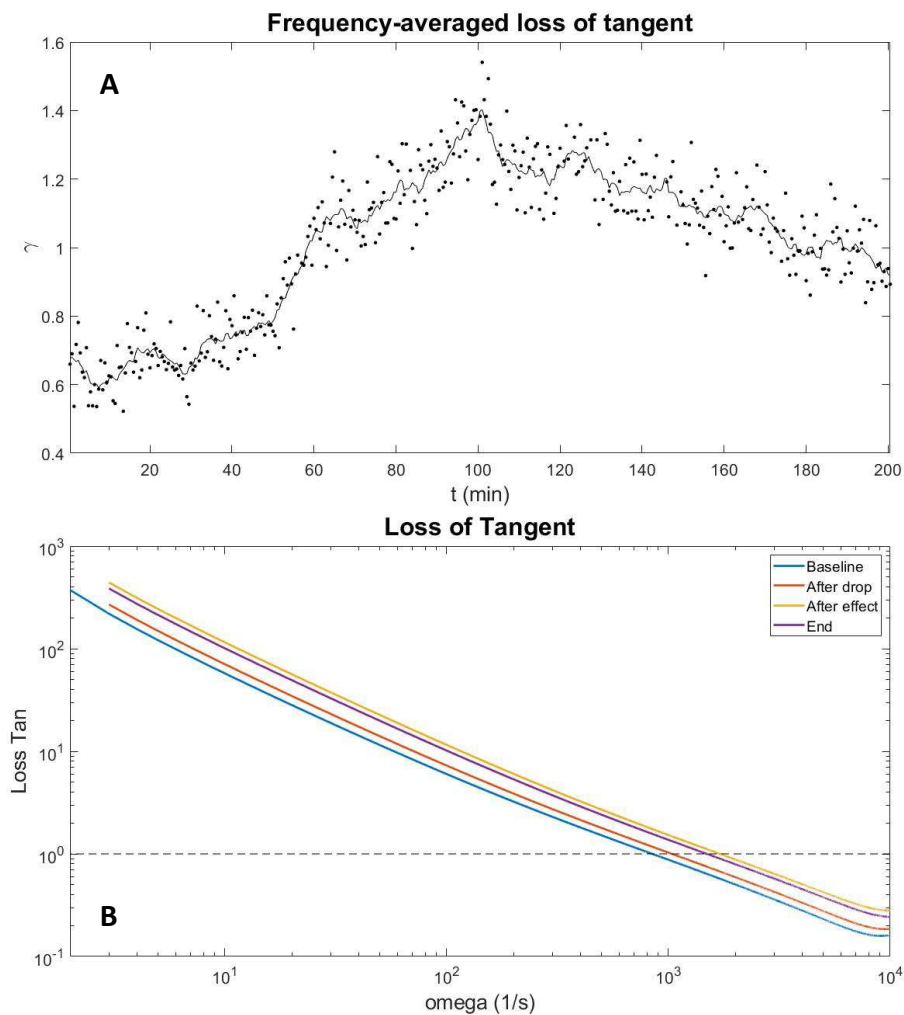


**Figure 4.16:** (A) Frequency-averaged loss of tangent. (B) Time-averaged loss of tangents during baseline measurements (blue line), after drug administration (red), after drug effect (yellow) and at the end of the experiment (violet).

## 5 CONCLUSIONS

Based on the presented results it is possible to draw the following conclusions:

- The platform detects statistically significant differences in normal and cancerous cell lines elasticities;
- The platform also shows differences between different cell states in the same cell line, although this is less evident;
- Both single administration experiments present an increased scattering activity originated by the bigger-size components and a transition from a stiffer to a softer state after the drug administration;
- The multiple administration experiment shows a reduced scattering activity over time and, first stiffening followed by a progressive softening and an oscillating gamma parameter.

The overall results are in agreement with the literature: as stated above, pronounced differences between prostate normal and cancer cell lines were already reported in Ref. [74]. These differences can be due to the morphological changes that happen when a healthy cell turns into a pathological one, evidenced by its shape and the surface brushes [107]. Moreover, because of the cytoskeleton's role in determining the cell shape and because of its mechanical differences in the cell's elasticities are expected to occur if different shapes are present, also in the same cell population.

Regarding the cell elasticity after the drug administration, as stated previously a similar behavior was already found with Taxol: the transition to a softer state (in experiments 1 and 3) was seen for Ishikawa cells and for HeLa cells with a first stiffening followed by a softening (as in experiment 2), which was detected and reported in Ref. [106].

The photonic platform developed for this project is one of the possible ways to measure cells vibrations, dynamics and properties in a rapid and cost-efficient

manner. As alternatives to DLS, Atomic Force Microscopy (AFM) [75,106-109], nano-mechanical oscillators like cantilevers derived from AFM [110-112], resonant crystals [113] and other optical techniques [114,115] among others have been proposed for this purpose. These methods allow rapid testing, which is useful in investigating cellular properties and viability under different conditions, which include drug treatments. Their importance is expected to increase over the next several years. In particular, the photonic platform used in this project has the following advantages:

- is cost-effective;
- allows real-time monitoring for prolonged times (hours);
- gives fast results with respect to standard methods for drugs susceptibility testing;
- is non-invasive, so the prolonged measurement will not influence the cell state: this is a clear advantage with respect to AFM techniques that trigger cytoskeleton remodeling when applied for prolonged times [108];
- can be combined with microscope imaging: this is helpful for monitoring the change in elasticity, which reflects a change in the cell viability as demonstrated in ref. [112].

Because of these advantages this DLS platform is one of the most promising tools for the optimization of cancer chemotherapy, although more tests and probably some improvements are needed. In particular, new tests on Nocodazole could be useful to better see the dependence of cell state transition time on drug concentration, while tests on other drugs could be performed to understand if the platform works well also with them. Moreover, the coupling of the power spectrum results with more precise theoretical modeling would be useful to better understand the sub-cellular dynamics and the drug action and will be the topic of future research.

In conclusion, in the modern world in which medicine is evolving from a more general approach to the disease to the development of more patient-specific therapies, the hope is that this photonic platform will be used in the future as a

precise tool enabling achievement of this goal. In particular this technology can be used to optimize cancer chemotherapy also at the patient-specific level by using biopsied tissues. In addition, drug testing and drug resistance experiments can be conducted not only on cancer, but possible involving bacteria, for which drug resistance is a well-known problem. Finally, coupling this technique with rational drug design could strongly reduce times and costs of drug discovery and development.

## APPENDIX 1: TUBULIN POLYMERIZATION MODEL IN VITRO

### Experimental procedure

As stated in section 1.4 MT polymerization is a complex phenomenon that involves several steps and is characterized by the so-called dynamic instability, for which the MT alternates periods of growing and shrinking in a stochastic manner. In addition, several factors influence the MT's dynamics, which can be therefore regulated by the cell.

Tubulin polymerization in vitro can be studied with different techniques, included DLS, so an experiment is performed in order to study this phenomenon. The workflow is the following:

- 45  $\mu\text{M}$  of Tubulin and 1 mM of Guanosine triphosphate (GTP) are put in suspension in a cuvette with BRB80 medium, initially in ice;
- The cuvette is then put in a thermal chamber for a thermal stabilization period of 10 minutes at 2° C;
- During this period a MMF like the one described in section 2.2 is put in the suspension;
- After the thermal stabilization baseline measurements at 2° C are taken for 3 minutes using DLS, which principles are explained in section 2.3;
- Once passed 3 minutes the temperature is rapidly increased to 37° C by the temperature chamber and the polymerization process is measured for 2 hours.

The recorded quantities are the same described in section 2.3. In particular, to study the polymerization process one has to look at the  $\beta$  parameter, which is analogous to the turbidity usually used to measure this phenomenon [32,116]. The recorded beta is shown in Figure A1.1.

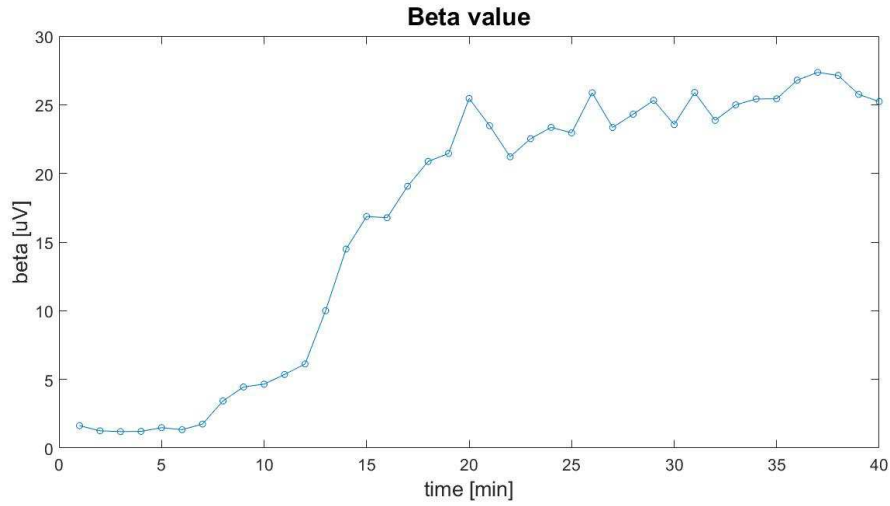
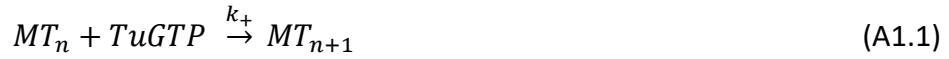


**Figure A1.1:** Beta value recorded during the experiment.

## Tubulin polymerization model

The tubulin polymerization model developed for this study accounts for four chemical reactions:

- MT growth:



- MT nucleation:



- MT shortening:



- Tu-GTP regeneration from Tu-GDP:



Where  $MT_n$  is the MT formed by  $n$  dimers,  $TuGTP$  and  $TuGDP$  are the tubulin bounded with GTP and GDP respectively and  $k_+$ ,  $k_n$ ,  $k_-$  and  $k_r$  are the reaction constants for the growing, nucleation, shortening and regeneration reactions respectively. According to this model the polymerization occurs in two steps: first there is a nucleation reaction in which a nucleus, assumed made by only one dimer for simplicity, is formed. Then dimers attach to this nucleus to make the MT growth. When the transition to a shortening phase occurs, the MT loses

dimers according to reaction (A1.3) and releases them as tubulin-GDP complexes. Reaction (A1.4) allows regeneration of GTP from GDP to ensure that dimers, once released, can polymerize again.

Since the fitted data come only from the beta plot, which represents the assembled tubulin, fitting for all the rate constants with one model is not possible because of the lack of information. To overcome this problem a “divide and conquer” approach, in which different models are developed in order to estimate one constant at the time, is used. This procedure reflects the strategy used in [117].

Firstly only the MT growth is taken into account: this means that assuming all free initial tubulin bound to GTP the only reactions that are considered are (A1.1) and (A1.2). The value of the association rate  $k_+$  is set equal to  $4.5 \mu\text{M}^{-1}\text{s}^{-1}$  from literature [116], so the only unknown is the nucleation constant  $k_n$ . The fitting model is the one developed in [118], for which, assuming that only one dimer is required for nucleation, we have:

$$c(t) = c_0 (\cosh(\sqrt{k_n k_+ c_0 / 2} t))^{-2} \quad (\text{A1.5})$$

Where  $c(t)$  is the monomer concentration as a function of time and  $c_0$  its initial value. Eq. (A1.5) leads to:

$$\frac{\beta}{\beta_\infty} = 1 - (\cosh(\sqrt{k_n k_+ c_0 / 2} t))^{-2} \quad (\text{A1.6})$$

From eq. (A1.6) is clear that the fitting is done with non-dimensional beta: that is because the proportionality constant between the beta parameter and the assembled tubulin is unknown so values are normalized with respect to the last recorded one ( $\beta_\infty$ ). Moreover the fitting is not done on the whole beta plot but the following modifications are applied:

- To remove the free tubulin signal from beta, which is noise, the average of the first 5 minutes is subtracted from data: during this time there are the thermal baseline and jump so no polymerization occurs;
- The fitting is done only from minute 5 (after thermal stabilization) to 15 (about 60% of the growth): in this way thermal effects are removed and the

only growth assumption becomes a good approximation because at the beginning of the growth depolymerisation is less frequent.

The fitting, which result is shown in Figure 7, leads to  $k_n = 2.3 \cdot 10^{-8} \text{ s}^{-1}$ .

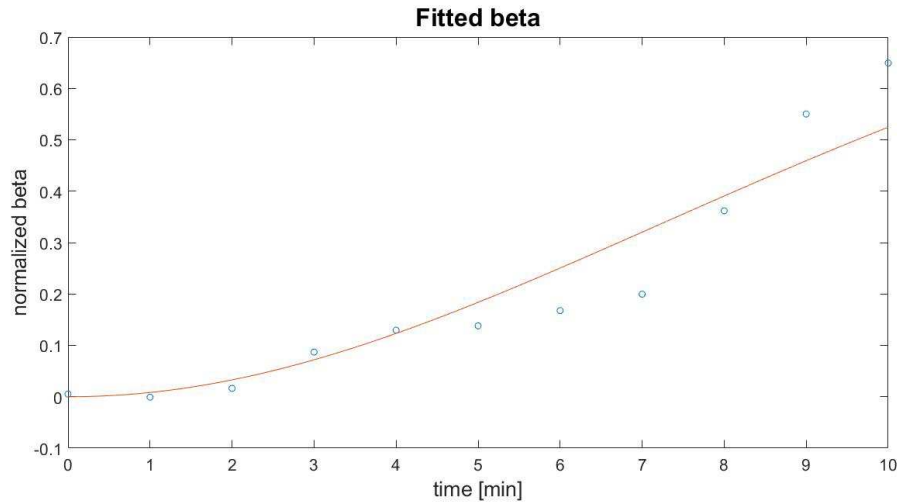


**Figure A1.2:** Normalized beta, fitted according to eq. (A1.6).

Now the complete model can be fitted to the whole beta data. For the fitting procedure the value of the depolymerisation constant  $k_-$  is set equal to  $24 \text{ s}^{-1}$  from literature [116] so the only remained constant to be estimated is the regeneration constant  $k_r$ . Assuming first order dependence of reaction from each reactant reactions from (A1.1) to (A1.4) correspond to the following system of differential equations:

$$\dot{N} = k_n T_t \quad (\text{A1.7})$$

$$\dot{T}_a = k_+ N T_t - k_- N + k_n T_t \quad (\text{A1.8})$$

$$\dot{T}_d = k_- N - k_r T_d \quad (\text{A1.9})$$

$$\dot{T}_t = -k_+ N T_t - k_n T_t + k_r T_d \quad (\text{A1.10})$$

Where  $N$ ,  $T_t$ ,  $T_a$ ,  $T_d$  are the molar concentrations of the number of MTs, the  $TuGTP$  complex, the assembled tubulin and the  $TuGDP$  complex, respectively, and  $\dot{N}$ ,  $\dot{T}_t$ ,  $\dot{T}_a$ ,  $\dot{T}_d$  are the corresponding variations over time. To fit the data all the previous considerations on the beta values are still valid, except for the fact

that now the fitting is made starting from the 5<sup>th</sup> minute to the end. The fitting leads to  $k_r = 0.0034 \text{ s}^{-1}$  and its result is shown in Figure A1.3.

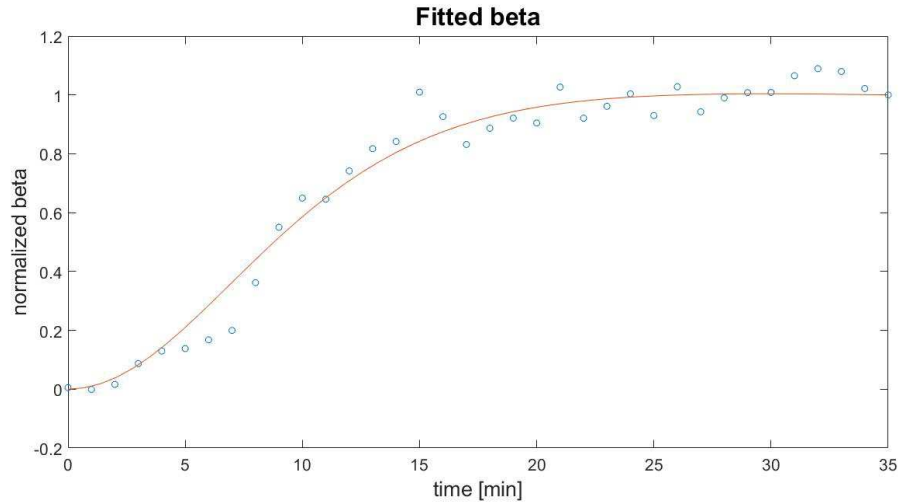


**Figure A1.3:** Normalized beta fitted according to the system of eqs. (A1.7)-(A1.10).

## Conclusions

This model is a good starting point to study tubulin polymerization in vitro and the effect of external environment or stimuli. In particular it was developed to study the effects of electromagnetic radiation, which will be the topic of a future work.

On the other hand, because of the strong differences in environmental conditions and the regulation of MTs dynamics by the cell, its direct application to the polymerization inside the cell is not giving satisfying results, although maybe more complex models based on this one could be developed in the future.

## APPENDIX 2: ORDERED WATER SYSTEM AROUND MICROTUBULES

### Introduction

Recently, the behavior of water at the interface with surfaces has gained a lot of attention [119]. In particular the existence of structural differences between bulk water and water at an interface with hydrophilic surfaces has been proposed by several research groups [120]. Pollack et al. experimentally demonstrated the presence of a water region near a Nafion surface from which microspheres in colloidal suspension are excluded, which was made clear by observations under the microscope [121]. This interface has been termed the exclusion zone (EZ). The EZ water has been shown to extend for as far as hundreds of microns and it has different physical properties with respect to bulk water. In particular, it exhibits a higher refractive index and viscosity and it absorbs electromagnetic energy with a peak at 270 nm [122]. In addition, experiments showed that EZ water is negatively charged, exhibiting a local electrostatic potential of about -200 mV. While it also excludes protons, positive ions can significantly reduce its extension [123,124]. Finally, it has been demonstrated that electromagnetic radiation affects the size of the EZ: in particular, IR light is the most effective in expanding it [125,126]. Various explanations have been proposed to provide a physical mechanism for this phenomenon [120] including the hypothesis put forward by Pollack based on the existence of a fourth phase of water, with properties interpolating between those of ice and liquid water [122]. Nafion is negatively charged and the most effective way to see the EZ extending from its surface is to use negatively charged suspended particles. Other hydrophilic surfaces were tried as well and also neutral and positive particles were placed in colloidal suspensions, but these results were less pronounced [123], supporting

the fundamental role of electric interactions, in particular those between negative charges in solution.

If Pollack's hypothesis is correct, it could have major consequences for biological systems, many of which have hydrophilic surface and virtually all involve interactions with water molecules [122]. Among subcellular structures MTs represent excellent candidates for demonstrating effects of EZ water due to the fact that they form large negatively charged surfaces from which smaller molecules, such as other proteins and ions in the cytoplasm, are excluded. In particular, tubulin dimers are highly charged compared to other proteins, with a bare electric charge of about  $-52e$ , based on the 3RYF structure in the Protein Data Bank (PDB), valid at physiological pH [49]. About half of this charge is located on C-termini of both tubulin monomers.

If an EZ water layer forms around MTs in a similar way to that for Nafion, this would mean that chemical reactions and interactions with other components of the cytoplasm would be influenced by it because of the effects on electrical repulsion and this could also help explain part of the environmental effects on cellular behavior since, as mentioned above, ionic concentrations influence the EZ size. This could be the case, for example, of cancer cells because the tumor microenvironment is very different from the physiological one, as explained in section 1.3, and the environmental differences are also involved in the determination of the EZ size [127]. The so-called Warburg effect, which is prominently demonstrated in cancer cells, represents a switch in the major energy production from aerobic respiration to glycolysis even if in the absence of hypoxic conditions [16], has been suggested to be influenced by ordered water [128] and experimental results suggest that ordered water layers extension around mitochondria can be modulated by light and has implications in ATP synthesis [129–132]. Moreover, long-range static electric fields on the order of microns were measured from mitochondrial surfaces [133], suggesting that membranes or other highly charged structures can generate long-range interactions which could be involved in biomolecular recognition [134]. In

addition, other cytoplasmic ions, e.g.  $K^+$  and  $Mg^{2+}$ , influence MT polymerization [41-43] and since they also influence the EZ's size, their influence on repulsion forces could be linked to the reaction rates. Finally, it has been shown that tubes made from hydrophilic materials, when immersed in water, generate a flow through themselves [122]. Hence, since some biomolecules such as proteins can access the MT lumen [135,136] their motion inside it could be influenced by the EZ water.

The aim of this appendix is therefore to provide an estimation for the EZ water formed around MTs in order to study the repulsion of tubulin dimers from MTs, using an approach based on the linearized Poisson-Boltzmann (LPB) equation. Moreover, since tubulin can assemble into different structures including flat sheets and microtubules [137], the tubulin-tubulin and the tubulin-sheet interactions are also modelled. These results could finally help better understanding the environmental effects on protein interactions.

### Theoretical approach

A good model for the evolution of the EZ was recently proposed in ref. [127]. The approach is based on the 1-D Langevin equation:

$$m\ddot{x}(t) = F(x) - \xi\dot{x}(t) + f(t) \quad (\text{A2.1})$$

where the following symbols have been used:

- $F(x)$  represents the electric force felt by the molecule at a distance  $x$  to the surface;
- $\xi = 6\pi\eta a$  is the friction coefficient according to the Stokes approximation where  $\eta$  is the medium's viscosity and  $a$  is the particle radius;
- $f(t)$  is a stochastic force of zero mean value.

To fit the EZ evolution to the time-dependent data, the force was assumed to be in the following form [127]:

$$\frac{F(x)}{\xi} = Ke^{-\kappa x} \quad (\text{A2.2})$$

While the authors have not elaborated on the origin of this force, they stated that it is related to an electric field experienced by the molecule and the values for  $K$  and  $\kappa$  were obtained by fitting the data according to the analytical solution of equation (A2.1) [127].

The force is very similar to the one obtained from the Poisson-Boltzmann (PB) equation because of the following properties: (a) it leads to an exponential decay over time [127], and (b) it generates ionic screening effects [123,127]. Moreover, the force field within the EZ was experimentally measured, revealing a decreasing value of the force as a function of distance [138]. The main difference is the length scale involved: the PB effect is expected to die down over a few microns while the EZ extent can reach hundreds of microns or even millimetres. Since the ordered water layers extension in cell seem to be in the nanometer scale [128,129] the PB effect could be a starting point to model the EZ phenomenon in biological environments and it was also used for the Nafion case [139]. We start these considerations, given the linearized PB (LPB) equation derived in [54] for the voltage  $V$ :

$$\nabla \cdot (\varepsilon_r \nabla V) = \frac{2eN_A c_s}{\varepsilon_0} \frac{eV}{k_B T} \quad (\text{A2.3})$$

in which  $\varepsilon_0$  and  $\varepsilon_r$  are the vacuum and relative permittivity, respectively,  $e$  is the elementary charge,  $N_A$  is the Avogadro number,  $c_s$  is the solution's ionic concentration,  $k_B$  is the Boltzmann constant and  $T$  is the absolute temperature. Since eq. (A2.3) has an analytical solution for particular geometries, the MT-tubulin, tubulin-tubulin and tubulin-sheet interactions are studied for two vastly different KCl concentrations (10 and 160 mM) in cytoplasm ( $\eta = 3 \cdot 10^{-3}$  Pa\*s,  $\varepsilon_r = 78.3$ ) at  $T = 20^\circ\text{C}$ , according to the following workflow:

- Find an analytical solution of the LPB (eq. (A2.3)) to obtain the electric field  $E(x)$  around the repelling surface;
- Obtain an estimate of the force  $F(x)$  acting on the tubulin dimer according to the formula:

$$F(x) = Q_{eff} E(x) \quad (\text{A2.4})$$

where  $Q_{eff}$  is the effective charge of the tubulin dimer at a given ionic concentration, according to [54];

- Find a numerical solution of the equation:

$$m\ddot{x}(t) = F(x) - \xi\dot{x}(t) \quad (A2.5)$$

and an estimation of the EZ. Eq. (A2.5) describes the motion of a single tubulin probe repelled from a surface and is supposed to provide the estimation of the EZ evolution over time, in a similar way as in [127];

- Generate an estimate of the involved energy as a function of the distance by multiplying the voltage with the tubulin effective charge and calculating the difference with respect to the starting position.

### Microtubules - tubulin interaction

Considering the MT as an infinite cylinder eq. (A2.3) for the voltage around the MT expressed in cylindrical coordinates becomes [54]:

$$\frac{1}{r} \frac{d}{dr} \left( r \epsilon_r \frac{dV}{dr} \right) = \frac{2eN_A c_s}{\epsilon_0} \frac{eV}{k_B T} \quad (A2.6)$$

Applying the same boundary conditions as in ref. [54], leads to the following solution for the voltage around the MT:

$$V(r) = \frac{\sigma \lambda_D}{\epsilon_0 \epsilon_r} \frac{R}{R+d} \frac{K_0(r/\lambda_D)}{K_1((R+d)/\lambda_D)} \quad (A2.7)$$

which subsequently leads to the electric field distribution as a function of radius:

$$E(r) = \frac{\sigma}{\epsilon_0 \epsilon_r} \frac{R}{R+d} \frac{K_1(r/\lambda_D)}{K_1((R+d)/\lambda_D)} \quad (A2.8)$$

In equations (A2.7) and (A2.8)  $R$  is the MT's external radius (12.5 nm),  $d$  is the thickness of the Stern layer (0.33 nm, equal to the  $K^+$  ion radius, used as correction factor for ionic size [54]),  $K_0$  and  $K_1$  are the modified Bessel functions of the second kind of zeroth and first order, respectively,  $\sigma$  is the surface charge density and  $\lambda_D$  the Debye length, calculated as:

$$\lambda_D = \frac{1}{\kappa} = \sqrt{\frac{\epsilon_0 \epsilon_r k_B T}{2N_A c_s e^2}} \quad (A2.9)$$

To use cylindrical geometry and take into account the charge of the external surface and the charge of the C-termini, which protrude from the MT, two estimations for the surface charge can be made as follows:

$$\sigma = \sigma_{out} \frac{A_{out}}{A_{tot}} + \sigma_{CT} \frac{2A_{CT}}{A_{tot}} = -0.102 \frac{C}{m^2} \quad (A2.10)$$

$$\sigma = \frac{Q_{out} + 2Q_{CT}}{A_{out}} = -0.156 \frac{C}{m^2} \quad (A2.11)$$

In formula (A2.10) an estimate is made recalling that  $A = Q/\sigma$  and assuming a charge of -25e for the outer surface and -11e for each C-terminus [54]. The tubulin dimer is modelled as a sphere of radius  $a = 2.71$  nm equivalent to an ellipsoid of semi axis 2x2.5x4 nm. Eq. (A2.5) is numerically solved assuming as initial conditions  $r(0) = d$  or  $r(0) = a$  and  $\dot{r}(0) = 0$  for both  $\sigma$  and for concentrations of 10 and 160 mM. Having estimated the EZ, the corresponding electrostatic energy variation is:

$$U(r) = Q_{eff} \frac{\sigma \lambda_D}{\epsilon_0 \epsilon_r} \frac{R}{R+d} \frac{K_0(r/\lambda_D)}{K_1((R+d)/\lambda_D)} \quad (A2.12)$$

where  $Q_{eff}$  is the effective charge of the tubulin dimer in the solution, estimated from [54] equal to -17e for 10 mM concentration and -29e for 160 mM one. The energy variation at a distance  $r$  is calculated by subtracting the value of the energy at the starting point, from the energy value at  $r$ , both calculated with eq. (A2.12). Results for the surface charge estimated according to eq. (A2.10) are shown in Figures A2.1-A2.4, while calculations made using the surface charge estimated according to (A2.11) are shown in Figures A2.5-A2.8.

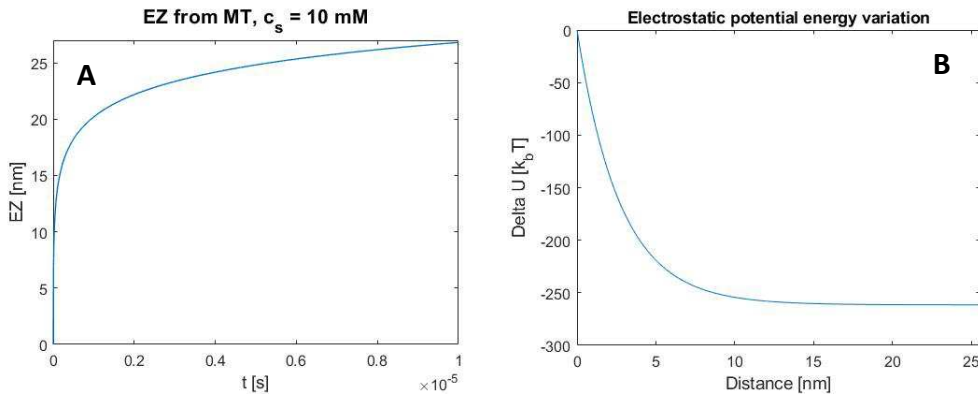


**Figure A2.1:** (A) EZ from MT at 10 mM. (B) Electrostatic potential energy variation.  $r(0) = d$ .

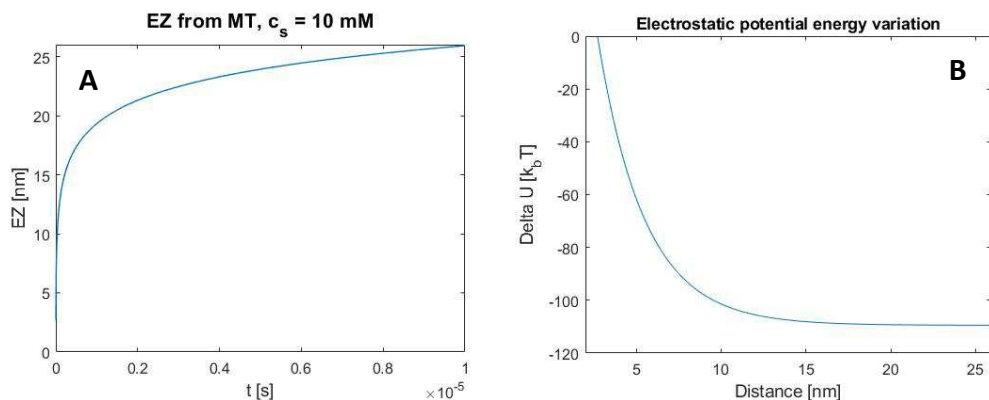


**Figure A2.2:** (A) EZ from MT at 10 mM. (B) Electrostatic potential energy variation.  $r(0) = a$ .

Figures A2.1 and A2.2, in which the ion concentration is assumed 10 mM, illustrate that in both cases the EZ size is about 25 nm and the timescale involved is on the order of  $\mu\text{s}$ , so the process is faster than the one with Nafion. The energy variation is much lower if the considered starting point is the particle radius: that is due to the fact that the Debye length at this concentration is about 3 nm, so the energy decay in the first nm away from the MT surface is important. According to Figure 3, the energy involved in the process is about  $-100 k_B T$ , which is a value comparable to the estimations of the free energy change involved in transferring a dimer from the MT lattice to the surrounding medium [140,141].

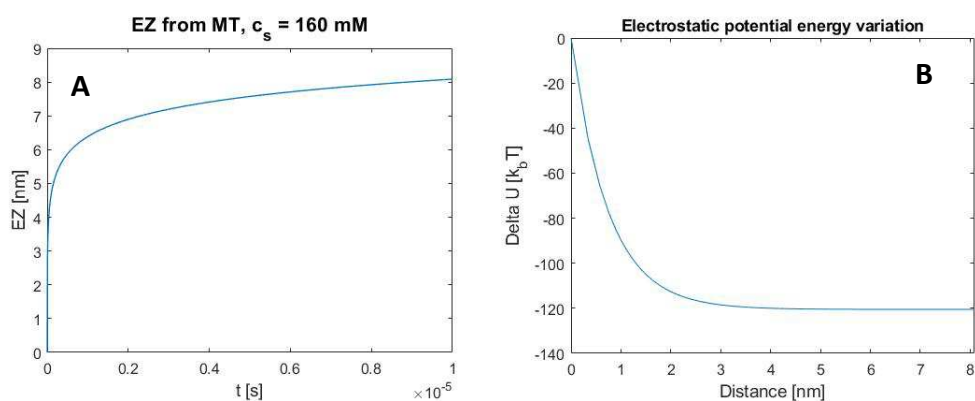


**Figure A2.3:** (A) EZ from MT at 160 mM. (B) Electrostatic potential energy variation.  $r(0) = d$ .

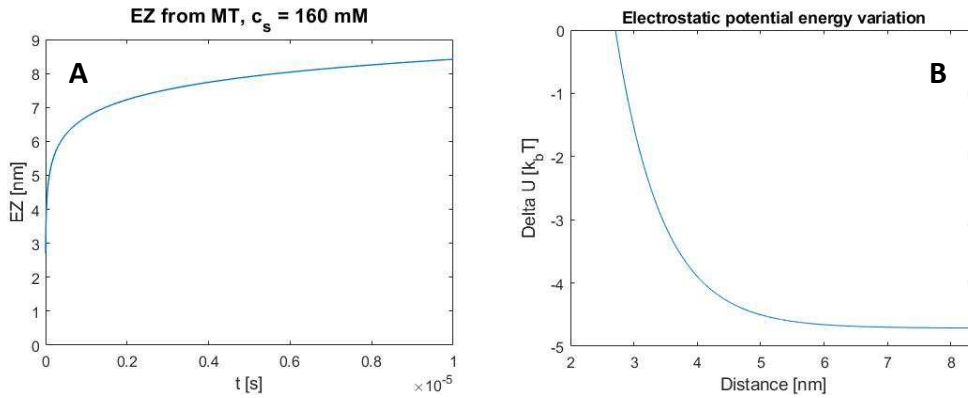


**Figure A2.4:** (A) EZ from MT at 160 mM. (B) Electrostatic potential energy variation.  $r(0) = a$ .

Figures A2.3 and A2.4 show the simulation results for  $[KCl] = 160$  mM. The timescale is the same but this time the EZ is lower and this is due to the fact that at higher ions concentrations the screening is stronger and the EZ is reduced. This reflects also on the energy estimations: now the Debye length is about 7.5 angstroms so the potential decays faster and the energy estimated is very low if  $r(0)$  is assumed equal to the tubulin radius, while values found for  $r(0) = d$  are important.

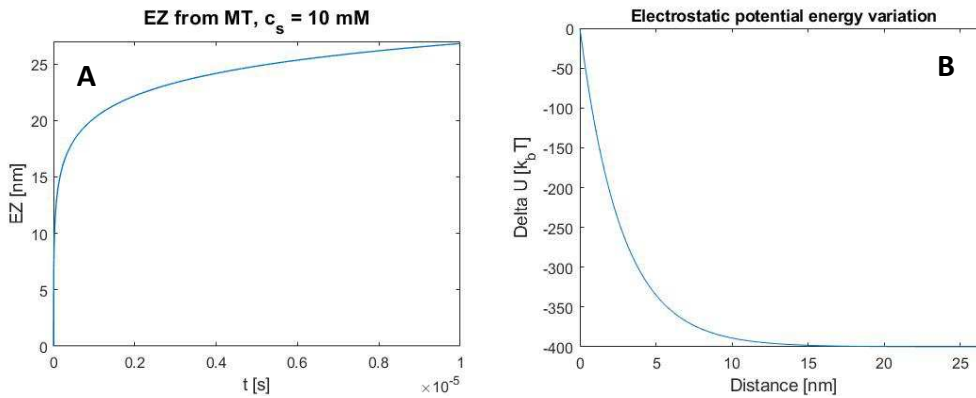


**Figure A2.5:** (A) EZ from MT at 10 mM. (B) Electrostatic potential energy variation.  $r(0) = d$ .

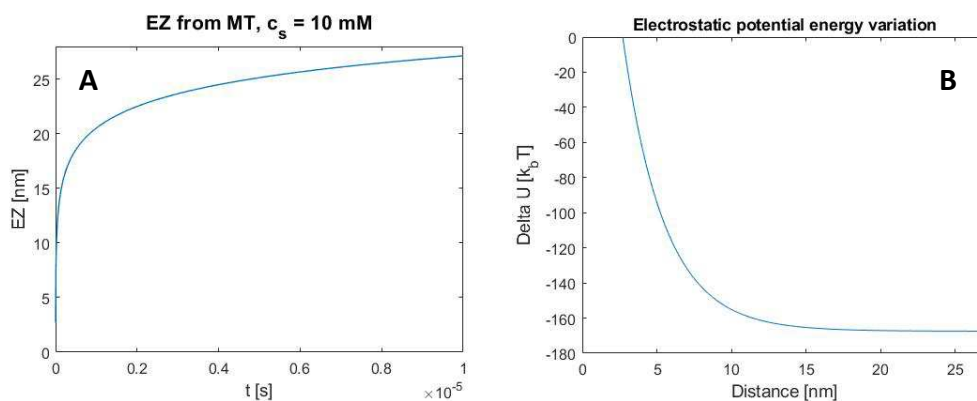


Figure A2.6: (A) EZ from MT at 10 mM. (B) Electrostatic potential energy variation.  $r(0) = a$ .

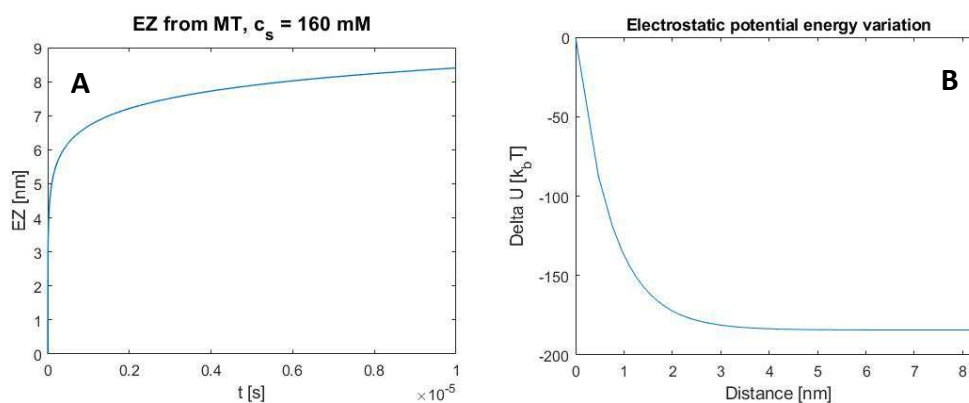


Figure A2.7: (A) EZ from MT at 160 mM. (B) Electrostatic potential energy variation.  $r(0) = a$ .

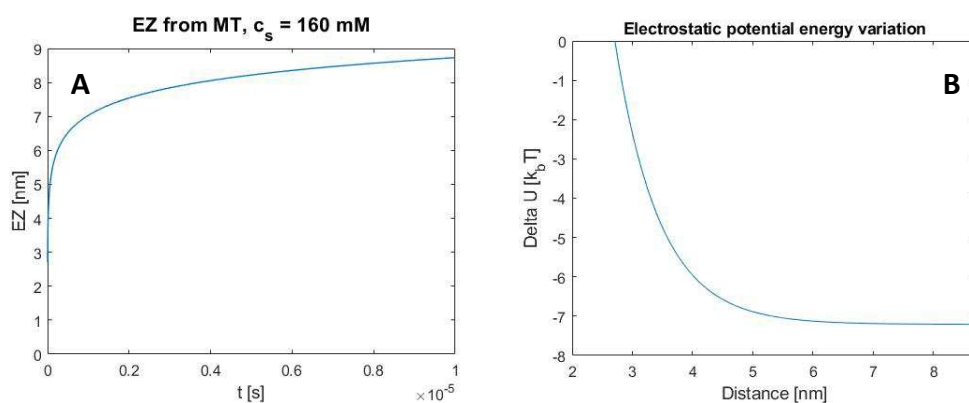


Figure A2.8: (A) EZ from MT at 160 mM. (B) Electrostatic potential energy variation.  $r(0) = a$ .

Results for the surface charge density estimated according to eq. (A2.11) are shown in Figures A2.5-A2.8. It can be seen that the EZ estimated with this  $\sigma$  are somewhat higher than the ones obtained using the estimation of eq. (A2.10). The

major difference is instead in the energies involved: since  $U(r)$  is proportional to the surface charge density an estimation, which provides a value 1.5 times greater will be reflected in an analogous result for the energy variation.

### Tubulin - tubulin interaction

To study the interaction between two tubulin dimers is convenient to model them again as spheres of radii 2.71 nm in order to apply a spherical symmetry approximation. The LPB equation expressing the voltage around the tubulin dimer in spherical coordinates becomes:

$$\frac{1}{r^2} \frac{d}{dr} \left( \epsilon_r r^2 \frac{dV}{dr} \right) = \frac{2e^2 N_{ACS}}{\epsilon_0 k_B T} V \quad (\text{A2.13})$$

By applying Gauss' law at the Stern layer ( $r = R+d$ ) we find:

$$-\frac{dV}{dr} = \frac{\sigma}{\epsilon_0 \epsilon_r} \frac{R^2}{(R+d)^2} \quad (\text{A2.14})$$

As a second boundary condition we suppose the electric field to be null at infinity. These two conditions lead to the following analytical solution:

$$V(r) = \frac{\sigma}{\epsilon_0 \epsilon_r} \frac{R^2}{(R+d)^2} r^{-1/2} \frac{K_{1/2}(r/\lambda_D)}{g(R+d)} \quad (\text{A2.15})$$

which leads to the electric field's radial distribution given by:

$$E(r) = \frac{\sigma}{\epsilon_0 \epsilon_r} \frac{R^2}{(R+d)^2} \frac{g(r)}{g(R+d)} \quad (\text{A2.16})$$

where the function  $g(z)$  is defined as:

$$g(z) = \left\{ \frac{z^{-3/2}}{2} K_{1/2}(z/\lambda_D) + \frac{r^{-1/2}}{\lambda_D} \left[ K_{3/2}(z/\lambda_D) - \frac{\lambda_D}{2z} K_{1/2}(z/\lambda_D) \right] \right\} \quad (\text{A2.17})$$

In Formulas (A2.15)-(A2.18)  $R$  is the tubulin radius,  $K_i$  are the modified Bessel functions of the  $i$ -th order and the surface charge is calculated as:

$$\sigma = \frac{Q_{bare}}{4\pi R^2} = -0.090 \frac{C}{m^2} \quad (\text{A2.18})$$

where the bare charge of the tubulin dimer is assumed as  $Q_{bare} = -52e$ . Now the potential energy is:

$$U(r) = Q_{eff} \frac{\sigma}{\epsilon_0 \epsilon_r} \frac{R^2}{(R+d)^2} r^{-1/2} \frac{K_{1/2}(r/\lambda_D)}{g(R+d)} \quad (\text{A2.19})$$

Here, both  $Q_{eff}$  and the energy variation are estimated as before. Simulations are performed with the same initial conditions as before and the results of our

simulations are shown in Figures A2.9-A2.12. Figures A2.9 and A2.10 refer to an ionic concentration of 10 mM. In both the EZ size extends almost to 20 nm over 10  $\mu$ s, so with respect to the MT-tubulin interaction at the same ionic concentration the repulsion is lower and that is valid also for the energies involved.

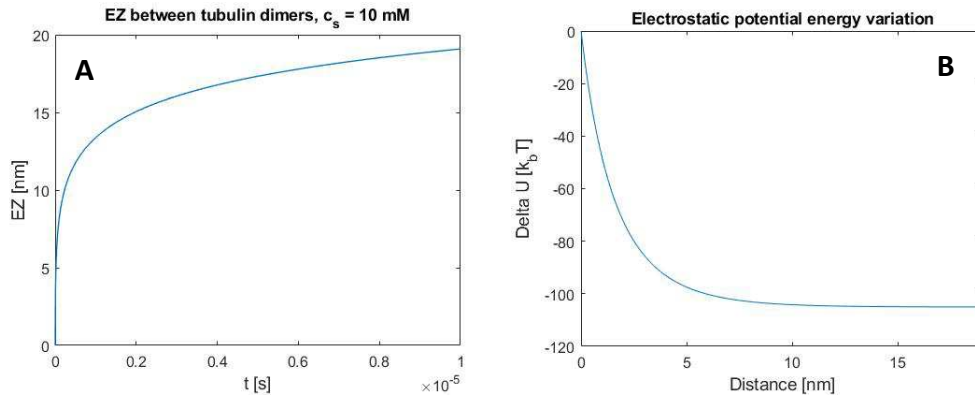


**Figure A2.9:** (A) EZ between tubulin dimers at 10 mM. (B) Electrostatic potential energy variation.  $r(0) = d$ .

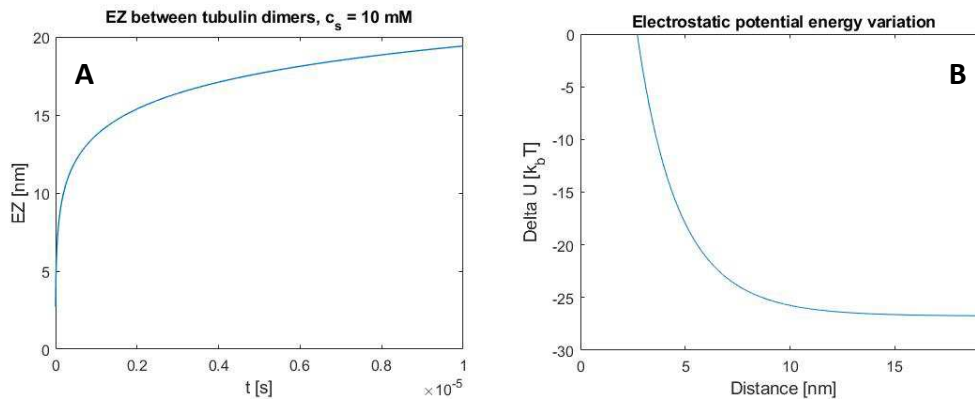


**Figure A2.10:** (A) EZ between tubulin dimers at 10 mM. (B) Electrostatic potential energy variation.  $r(0) = a$ .

Figures A2.11 and A2.12 show the results for an ionic concentration of 160 mM. Again, the electrostatic repulsion leads to a lower EZ with respect to the one estimated for the MT-tubulin interaction. Moreover, as before the difference in the Debye length of the solutions is reflected in the energy variations, such that

the assumption of  $r(0) = a$  leads to a very low energy release with respect to the other values.

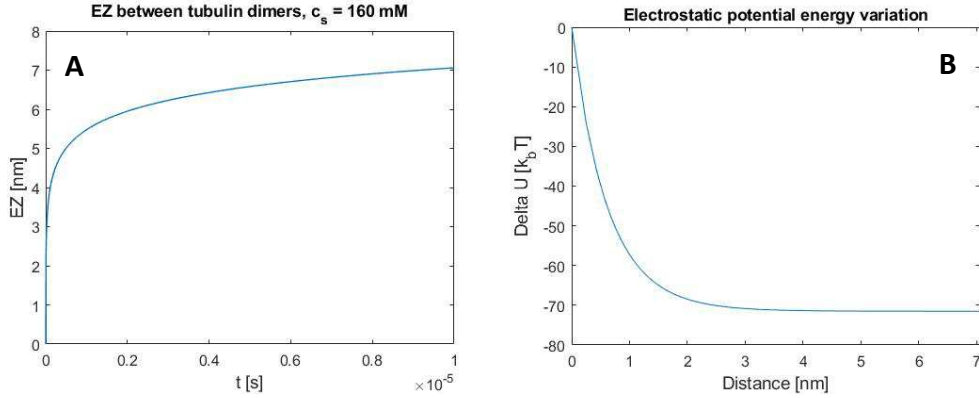


**Figure A2.11:** (A) EZ between tubulin dimers at 160 mM. (B) Electrostatic potential energy variation.  $r(0) = d$ .

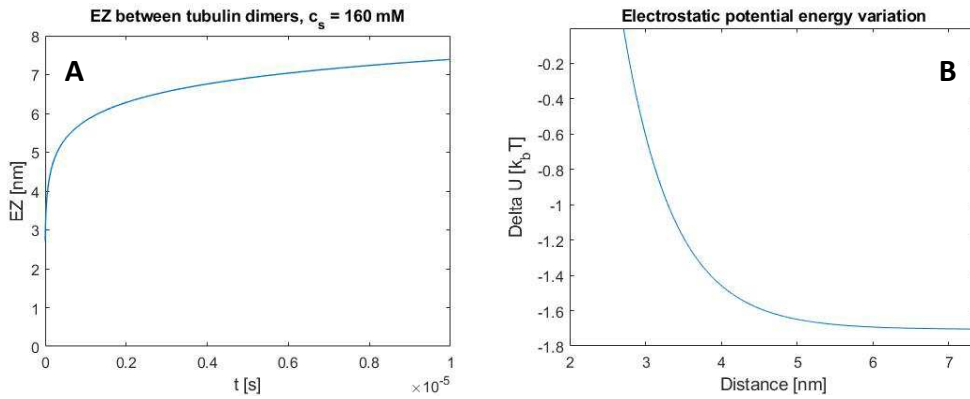


**Figure A2.12:** (A) EZ between tubulin dimers at 160 mM. (B) Electrostatic potential energy variation.  $r(0) = a$ .

### Tubulin sheet - tubulin interaction

In this case the LPB equation is used to express the voltage generated by the planar tubulin sheet in Cartesian coordinates. Considering the sheet as an infinite plane allows to have a 1-D equation for the potential:

$$\epsilon_r \frac{d^2 V}{dx^2} = \frac{2eN_A c_s}{\epsilon_0 \epsilon_r} \frac{eV}{k_B T} \quad (\text{A2.20})$$

By applying Gauss' law at  $x = d$  and assuming the electric field to be null for  $x$  going to infinity as boundary conditions, the analytical solution of eq. (A2.20) is found as:

$$V(x) = \frac{\sigma\lambda_D}{2\varepsilon_0\varepsilon_r} e^{-(x-d)/\lambda_D} \quad (\text{A2.21})$$

which leads to the electric field distribution as a function of distance given by:

$$E(x) = \frac{\sigma}{2\varepsilon_0\varepsilon_r} e^{-(x-d)/\lambda_D} \quad (\text{A2.22})$$

In this case the surface charge density is  $\sigma = -0.090 \text{ C/m}^2$ , calculated in the same way as in the tubulin-tubulin interaction. Finally, the electrostatic energy becomes:

$$U(r) = q_{eff} \frac{\sigma\lambda_D}{2\varepsilon_0\varepsilon_r} e^{-(x-d)/\lambda_D} \quad (\text{A2.23})$$

where the effective charge of the tubulin dimer is estimated as before. The same procedure as in the previous cases is followed to calculate the energy variation and the same initial conditions as in the previous cases are applied. Results for  $[\text{KCl}] = 10 \text{ mM}$  are shown in Figures A2.13 and A2.14. In this case, the EZ size is close to the one obtained in the MT-tubulin interaction, while the energies involved are about one half of those in that case. The majority of the process takes place again in the first microseconds and the Debye length makes the energy variation important in both cases.

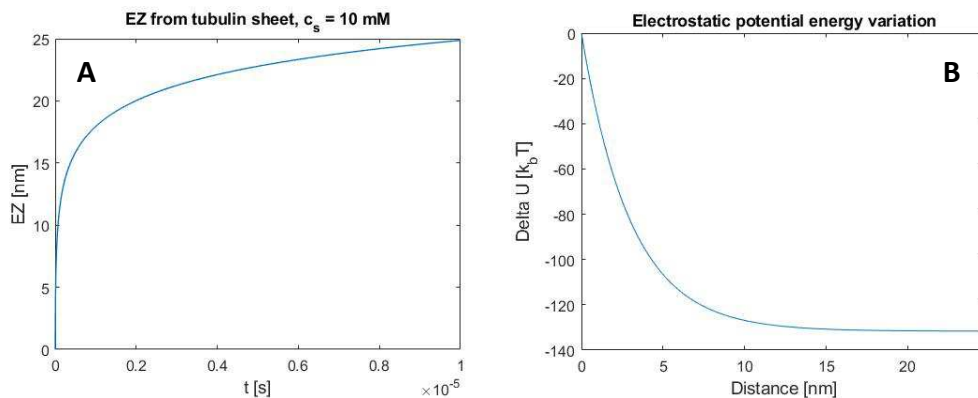


**Figure A2.13:** (A) EZ from tubulin sheet at 10 mM. (B) Electrostatic potential energy variation.  $x(0) = d$ .

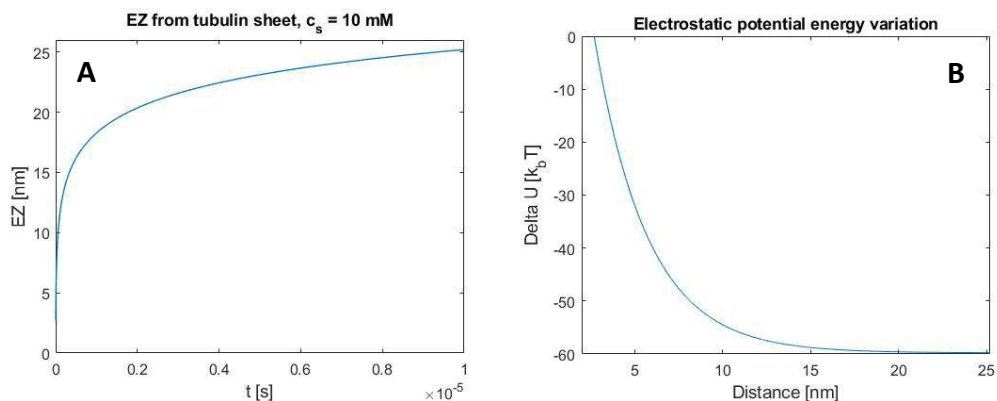


**Figure A2.14:** (A) EZ from tubulin sheet at 10 mM. (B) Electrostatic potential energy variation.  $x(0) = a$ .

Figures A2.15 and A2.16 show results for  $[\text{KCl}] = 160 \text{ mM}$ . Again, the EZ extension is similar to the one obtained for the MT-tubulin interaction and the timescale are the same. As in all other cases, the decreased Debye length due to the increased ionic screening leads to a very low energy variation for the case in which the starting position is assumed equal to the tubulin radius.

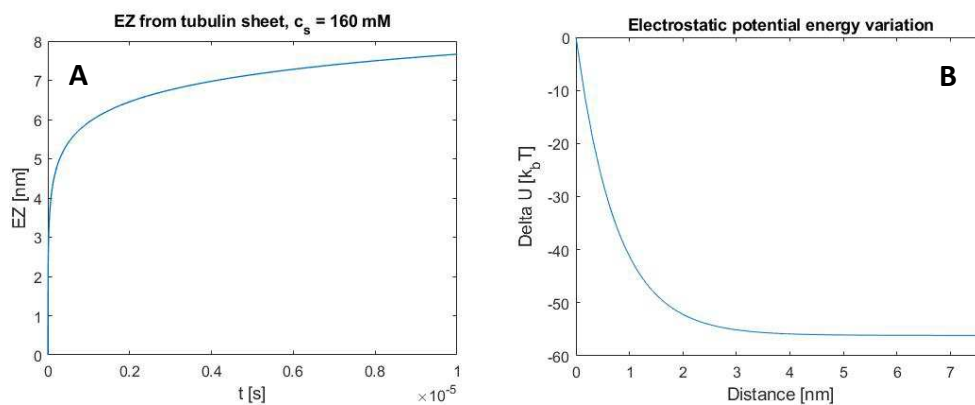


**Figure A2.15:** (A) EZ from tubulin sheet at 160 mM. (B) Electrostatic potential energy variation.  $x(0) = d$ .

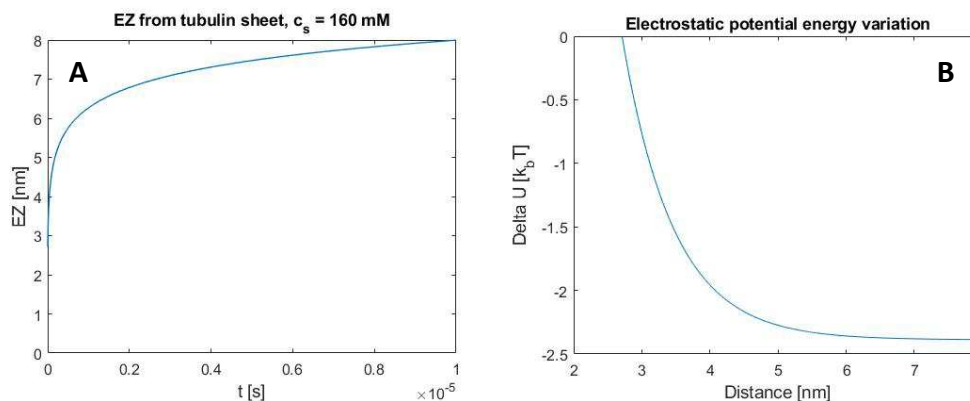


**Figure A2.16:** (A) EZ from tubulin sheet at 160 mM. (B) Electrostatic potential energy variation.  $x(0) = a$ .

## Conclusions

Based on the results of the simulations reported in this appendix, it is possible to state the following predictions regarding the effects of EZ water on microtubules in ionic solutions:

- The ionic screening effect means that at a lower KCl concentration the counterion screening is reduced so the voltage is higher. This leads to a stronger force felt by the particle and thus to a larger EZ, which is consistent with experimental results reported for Nafion [123,127].
- The evolution of EZ around MTs is very fast at the beginning of the process (a couple of  $\mu$ s) and then it slows down significantly, meaning that the process has a timescale on the order of tens of microseconds.
- The energy released by the system varies from several  $k_B T$  to hundreds of  $k_B T$  depending on the simulation conditions. In particular most of the energy is released in the first three nanometers and this is due to the fact that the Debye length, which is the decay constant associated to the PB potential, is of the order of one nanometer.

The simulations reported here were made using the LPB equation, which is a good approximation for higher concentrations but leads to an overestimation of the voltage for lower ones.

A possible explanation of the EZ extension, i.e. that EZ with Nafion is greater than expected from the PB equation, could be related to the fact that EZ water also excludes protons, leading to the formation of a PZ zone afterwards [126]. This could also happen to all the other positive ions in the solution, leading to a zone in which ion concentrations are very low. This fact would imply a higher local Debye length and as a consequence a reduced screening effect and a longer range of interaction. Probably this exclusion of the positive ions is not as efficient as the exclusion of negative particles and so some positive ions penetrate into the EZ, which would explain why the addition of positive ions reduces the EZ and why the potential in the EZ is more screened when positive ions are added to the solution [123]. In addition to this, since the EZ has a higher refractive index than water [122], it also has an higher relative dielectric constant and thus a larger Debye length (although this effect on the Debye length is very small).

Another characteristic of the EZ is that radiant energy, especially due to IR radiation, enhances EZ extension [125,126]. This could be explained by the fact that the radiation provides energy for the charge separation, reducing the local concentration even more. In addition, from recently reported aquaphotomics experiments it is possible to conclude that radiation changes the molecular network of water [142]. Aquaphotomics is a new discipline in which light with different frequencies is used to investigate the structure of water [143,144] and thus infer the system's intrinsic properties. This discipline could be of interest to test hypotheses regarding the EZ formation not only in the case of Nafion but also for other compounds, including biological polymers like MTs. These results coupled with experiments could help explaining environmental influence on MTs polymerization. In particular the role of ions, that as said before influence the process a lot [41-43]: part of their effect can be due to the charge screening showed here. In addition electromagnetic radiation can generate collective excitations and long-range interactions not only in MTs but also in other biological molecules [145-147] and can act on MTs polymerization [148]: these effects could be related to the modifications of the surrounding water observed

by Pollack. Electromagnetic radiation seems also to influence drug absorption by the cell by its action on interfacial water layers [149] so this appendix can provide a first insight on the role of light in chemotherapy. Finally, also heavy water ( $D_2O$ ) has effects on MTs polymerization [44,45,150] so if its properties influence the water ordering repulsions could change.

Finally, if such a depletion zone origins, a change in the refractive index around the MT is expected (this happens with Nafion [122]). The way in which the refractive index changes would help explaining the MT behaviour as an antenna. From recent results on local pH changes around MTs (unpublished data) we expect a gradual change of the refractive index which would imply the MT acting as a graded-index fiber for which the pH and the ionic concentration dependence are significant. Further investigations on the role of water in biological compound are therefore of great interest to understand how biological systems work because the water abundance in biological organisms makes it a fundamental element in life and its role is not yet fully understood.

## REFERENCES

- [1] Provisional Mortality Data — United States, 2020.  
<https://www.cdc.gov/mmwr/volumes/70/wr/mm7014e1.htm>
- [2] National Cancer Institute. <https://www.cancer.gov/>
- [3] American Association for Cancer Research – AACR Cancer Progress Report 2013. <https://www.cancerprogressreport.org>
- [4] Global Cancer Observatory. <https://gco.iarc.fr/>
- [5] Hopkins, A. L.; Mason, J. S.; Overington, J. P. Can we rationally design promiscuous drugs? *Current Opinion in Structural Biology* 2006, 16:127–136.
- [6] Sonnenschein, C.; Soto, A. M. *The Society of Cells: Cancer and Control of Cell Proliferation*. 1999.
- [7] Holohan, C.; Van Schaeybroeck, S.; Longley, D. B.; Johnston, P. G. Cancer drug resistance: an evolving paradigm. *Nature Reviews Cancer*, 2013, 13:714–726.
- [8] Mbeunkui, F.; Johann, D. J. Jr. Cancer and the tumor microenvironment: a review of an essential relationship. *Cancer Chemotherapy and Pharmacology*, 2009, 63:571–582.
- [9] Hanahan, D.; Weinberg, R. A.; *Hallmarks of Cancer: The Next Generation*. *Cell*, 2011, 144:646–674.
- [10] Hinck, L.; Nathke, I. Changes in cell and tissue organization in cancer of the breast and colon. *Current Opinion in Cell Biology*, 2014, 26:87-95.
- [11] Robbins, S. L.; Kumar, V. *Robbins Basic Pathology*. Saunders/Elsevier 2007.
- [12] Sobin, L. H. *The International Histological Classification of Tumours*. *Bulletin of the World Health Organization*. 1981, 59(6): 813–819.
- [13] MedlinePlus. <https://medlineplus.gov/benigntumors.html>
- [14] National Cancer Institute.  
<https://training.seer.cancer.gov/disease/cancer/>

- [15] Talmadge, J. E.; Fidler, I. J. AACR centennial series: the biology of cancer metastasis: historical perspective. *Cancer Research*, 2010, 70, 5649–5669.
- [16] Warburg, O. On the Origin of Cancer Cells. *Science*, 1956, 13(3191):309-314.
- [17] Gilbertson, R. J.; Rich, J. N. Making a tumour's bed: glioblastoma stem cells and the vascular niche. *Nature Reviews Cancer*, 2007, 7:733–736.
- [18] Ruoslahti, E. Specialization of tumour vasculature. *Nature Reviews Cancer*, 2002, 2:83–90.
- [19] Pietras, K; Östman, A. Hallmarks of cancer: Interactions with the tumor stroma. *Experimental Cell Research*, 2010, 316:1324–1331.
- [20] Grivennikov, S. I.; Greten, F. R.; Karin, M. Immunity, inflammation, and cancer. *Cell*, 2010, 140:883–899.
- [21] Matsumura, Y.; Maeda, H. A New Concept for Macromolecular Therapeutics in Cancer Chemotherapy: Mechanism of Tumor-tropic Accumulation of Proteins and the Antitumor Agent Smancs. *Cancer Research*, 1986, 46:6387-6392.
- [22] Maeda, H.; Nakamura, H.; Fang, J. The EPR effect for macromolecular drug delivery to solid tumors: Improvement of tumor uptake, lowering of systemic toxicity, and distinct tumor imaging in vivo. *Advanced Drug Delivery Reviews*, 2013, 65(1):71-79.
- [23] Heldin, C.-H.; Rubin, K.; Pietras, K.; Östman, A. High interstitial fluid pressure — an obstacle in cancer therapy. *Nature Reviews Cancer*, 2004, 4:806–813.
- [24] Hockel, M.; Vaupel, P. Tumor Hypoxia: Definitions and Current Clinical, Biologic, and Molecular Aspects. *Journal of the National Cancer Institute*, 2001, 93(4): 266–276.
- [25] Kizaka-Kondoh, S.; Inoue, M.; Harada, H.; Hiraoka, M. Tumor hypoxia: A target for selective cancer therapy. *Cancer Science*, 2005, 94(12):1021-1028.

- [26] Webb, B. A.; Chimenti, M.; Jacobson, M. P.; Barber, D. L. Dysregulated pH: a perfect storm for cancer progression. *Nature Reviews Cancer*, 2011, 11:671-677.
- [27] Quadir, M. A.; Morton, S. W.; Deng, Z. J.; Shopsowitz, K. E.; Murphy, R. P.; Epps III, T. H.; Hammond, P. T. PEG–Polypeptide Block Copolymers as pH-Responsive Endosome Solubilizing Drug Nanocarriers. *Molecular Pharmaceutics*, 2014, 11(7):2420–2430.
- [28] Wu, G.; Fang, Y.-Z.; Yang, S.; Lupton, J. R.; Turner, N. D. Glutathione Metabolism and Its Implications for Health. *The Journal of Nutrition*, 2004, 134(3):489-492.
- [29] Cheng, R.; Feng, F.; Meng, F.; Deng, C.; Feijen, J.; Zhong, Z. Glutathione-responsive nano-vehicles as a promising platform for targeted intracellular drug and gene delivery. *Journal of Controlled Release*, 2011, 152(1):2-12.
- [30] Sept, D.; Baker, N. A.; Mccammon, J. A. The physical basis of microtubule structure and stability. *Protein Science*, 2003, 12(10):2257-2261.
- [31] Mitchison, T.; Kirschner, M. Dynamic instability of microtubule growth. *Nature*, 1984, 312:237–242.
- [32] Johnson, K. A.; Borisy, G. G. Kinetic Analysis of Microtubule Self-assembly in Vitro. *Journal of Molecular Biology*, 1977, 117:1-31.
- [33] Margolis, R. L.; Wilson, L. Microtubule treadmill: what goes around comes around. *Bioessays*, 1998, 20:830–836.
- [34] Vale, R. D.; Coppin, C. M.; Malik, F.; Kull, F. J.; Milligan, R. A. Tubulin GTP hydrolysis influences the structure, mechanical properties, and kinesin-driven transport of microtubules. *Journal of Biological Chemistry*, 1994, 269:23769–23775
- [35] Melki, R.; Carlier, M. F.; Pantaloni, D.; Timasheff, S. N. Cold depolymerization of microtubules to double rings: geometric stabilization of assemblies. *Biochemistry*, 1989, 28:9143–9152.
- [36] Hyman, A. A.; Chretien, D.; Arnal, I.; Wade, R. H. Structural changes accompanying GTP hydrolysis in microtubules: information from a slowly

- hydrolyzable analogue guanylyl- (alpha,beta)-methylene-diphosphate. *Journal of Cell Biology*, 1995, 128:117–125.
- [37] Théry, M.; Blanchoin, L. Microtubule self-repair. *Current Opinion in Cell Biology*, 2021, 68:144–154.
- [38] Schaedel, L.; Triclin, S.; Chrétien, D.; Abrieu, A.; Aumeier, C.; Gaillard, J.; Blanchoin, L.; Théry, M.; John, K. Lattice defects induce microtubule self-renewal. *Nature Physics*, 2019, 15:830–838.
- [39] Brouhard, G. J.; Rice, L. M. Microtubule dynamics: an interplay of biochemistry and mechanics. *Nature Reviews Molecular Cell Biology*, 2018, 19:451–463.
- [40] Janke, C.; Bulinski, J. C. Post-translational regulation of the microtubule cytoskeleton: mechanisms and functions. *Nature reviews Molecular cell biology*, 2011, 12:773–786.
- [41] Olmsted, J. B.; Borisy, G. G. Characterization of Microtubule Assembly in Porcine Brain Extracts by Viscometry. *Biochemistry*, 1973, 12(21):4282-4289.
- [42] Borisy, G. G.; Marcum, J. M.; Olmsted, J. B.; Murphy, D. B.; Johnson, K. A. Purification of tubulin and associated high molecular weight proteins from porcine brain and characterization of microtubule assembly in vitro. *Annals of the New York Academy of Science*, 1975, 253(1):107-132.
- [43] Lee, J. C.; Timasheff, S. N. In Vitro Reconstitution of Calf Brain Microtubules: Effects of Solution Variables. *Biochemistry*, 1977, 16(8):1754-1764.
- [44] Chakrabarti, G.; Kim, S.; Gupta, M. L. Jr.; Barton, J. S.; Himes, R. H. Stabilization of Tubulin by Deuterium Oxide. *Biochemistry*, 1999, 38(10):3067–3072.
- [45] Panda, D.; Chakrabarti, G.; Hudson, J.; Pigg, K.; Miller, H. P.; Wilson, L.; Himes, R. H. Suppression of Microtubule Dynamic Instability and Treadmilling by Deuterium Oxide. *Biochemistry*, 2000, 39(17):5075–5081.
- [46] Tuszynski, J. A.; Luchko, T.; Portet, S.; Dixon, J. M.; Anisotropic elastic properties of microtubules. *The European Physical Journal E*, 2005, 17:29–35.

- [47] Hawkins, T.; Mirigian, M.; Selcuk Yasar, M.; Ross, J. L. Mechanics of microtubules. *Journal of biomechanics*, 2010, 43(1):23-30.
- [48] Kalra, A. P.; Eakins, B. B.; Patel, S. D.; Ciniero, G.; Rezania, V.; Shankar, K.; Tuszynski, J. A. All Wired Up: An Exploration of the Electrical Properties of Microtubules and Tubulin. *ACS Nano*, 2020, 14:16301–16320.
- [49] van den Heuvel, M. G. L.; de Graaff, M. P.; Lemay, S. G.; Dekker, C. Electrophoresis of individual microtubules in microchannels. *Proceedings of the National Academy of Science of the USA*, 2007, 104(19):7770-7775.
- [50] Sataric, M.; Ilic, D.; Ralevic, N.; Tuszynski, J. A. A nonlinear model of ionic wave propagation along microtubules. *European Biophysics Journal*, 2009, 38:637–647.
- [51] Priel, A.; Tuszynski, J. A. A nonlinear cable-like model of amplified ionic wave propagation along microtubules. *Europhysics Letters*, 2008, 83:68004.
- [52] Priel, A.; Ramos, A. J.; Tuszynski, J. A.; Cantiello, H. F. A biopolymer transistor: electrical amplification by microtubules. *Biophysical Journal*, 2006, 90:4639–4643.
- [53] Tuszynski, J. A.; Friesen, D.; Freedman, H.; Sbitnev, V. I.; Kim, H.; Santelices, I.; Kalra, A. P.; Patel, S. D.; Shankar, K.; Chua, L. O. Microtubules as sub-cellular memristors. *Scientific Reports*, 2020, 10:2108.
- [54] Eakins, B. B.; Patel, S. D.; Kalra, A. P.; Rezania, V.; Shankar, K.; Tuszynski, J. A. Modeling Microtubule Counterion Distributions and Conductivity Using the Poisson-Boltzmann Equation. *Frontiers in Molecular Biosciences*, 2021, 8:650757.
- [55] Hameroff, S.; Penrose, R. Consciousness in the universe A review of the ‘Orch OR’ theory. *Life Reviews*, 2014, 11:39-78.
- [56] Prosser, B. L.; Ward, C. W.; Lederer W. J. X-ROS signalling: Rapid mechano-chemo transduction in heart. *Science*, 2011, 333(6048):1440-1445.
- [57] Kerr, J. P.; Robison, P.; Shi, G.; Bogush, A. I.; Kempema, A. M.; Hexum, J. K.; Becerra, N.; Harki, D. A.; Martin, S. S.; Raiteri, R.; Prosser, B. L.; Ward, C.

- W. Detyrosinated microtubules modulate mechano-transduction in heart and skeletal muscle. *Nature Communication*, 2015, 6:8526.
- [58] Hein, S.; Kostin, S.; Heling, A.; Maeno, Y.; Schaper, J. The role of the cytoskeleton in heart failure. *Cardiovascular Research*, 2000, 45(2):273–278.
- [59] Jean, D. C.; Baas, P. W. It cuts two ways: microtubule loss during Alzheimer disease. *EMBO Journal*, 2013, 32:2900-2902.
- [60] Ren, Y.; Liu, W.; Jiang, H.; Jiang, Q.; Feng, J. Selective Vulnerability of Dopaminergic Neurons to Microtubule Depolymerization. *The Journal Of Biological Chemistry*, 2005, 280(40):34105–34112.
- [61] Kett, L. R.; Boassa, D.; Cheng-Ying Ho, C.; Rideout, H. J.; Hu, J.; Terada, M.; Ellisman, M.; Dauer, W. T. LRRK2 Parkinson disease mutations enhance its microtubule association. *Human Molecular Genetics*, 2002, 21(4):890–899.
- [62] Cermakova, P.; Eriksdotter, M.; Lund, L. H.; Winblad, B.; Religa, P.; Religa, D. Heart failure and Alzheimer’s disease. *Journal of Internal Medicine*, 2015(277):406–425.
- [63] Choku Takahashi, T.; Sato, H. Effects of Heavy Water (D20) on the Length of the Mitotic Period in Developing Sea Urchin Eggs. *Cell Structure and Function*, 1984, 8:357-365.
- [64] Jordan, M. A.; Wilson, L. Microtubules as a target for anticancer drugs. *Nature Reviews Cancer*, 2004, 4:253–265.
- [65] Stanton, R. A.; Gernert, K. M.; Nettles, J. H.; Aneja, R. Drugs That Target Dynamic Microtubules: A New Molecular Perspective. *Medicinal Research Reviews*, 2011, 31(3):443-481.
- [66] De Brabander, M. J.; Van de Velre, R. M. L.; Aerts, F. E. M.; Borgers, M.; Janssen, P. A. J. The Effects of Methyl [5-(2-Thienylcarbonyl)-1H-benzimidazol-2-yl]carbamate, (R 17934; NSC 238159), a New Synthetic Antitumoral Drug Interfering with Microtubules, on Mammalian Cells Cultured in Vitro. *Cancer Research*, 1976, 36(3):905-916.

- [67] Naaz, F.; Haider, M. R.; Shafi, S.; Shahar Yar, M. Anti-tubulin agents of natural origin: Targeting taxol, vinca, and colchicine binding domains. *European Journal of Medicinal Chemistry*, 2019, 171:310-331.
- [68] Downing, K. H. Structural basis for the interaction of tubulin with proteins and drugs that affect microtubule dynamics, *Annual Review of Cell and Developmental Biology*, 2000, 16:89–111.
- [69] Bai, R. L.; Pettit, G. R.; Hamel, E. Binding of dolastatin 10 to tubulin at a distinct site for peptide antimitotic agents near the exchangeable nucleotide and vinca alkaloid sites. *Journal of Biological Chemistry*, 1990, 265(28):17141-17149.
- [70] Rai, S. S.; Wolff, J. Localization of the vinblastine-binding site on  $\beta$ -tubulin. *Journal of Biological Chemistry*, 1996, 271:14707–11.
- [71] Uppuluri, S.; Knipling, L.; Sackett, D. L.; Wolff, J. 1993. Localization of the colchicine-binding site of tubulin. *Proceedings of the National Academy of Science of the USA*, 1993, 90:11598–502.
- [72] Bai, R.; Pei, X.; Boye, O.; Getanunt, Z.; Grover, S.; Bekisz, J.; Nguyen, N. Y.; Brossi, A.; Hamel, E. Identification of cysteine 354 of  $\beta$ -tubulin as part of the binding site for the A ring of colchicine. *Journal of Biological Chemistry*, 1996, 271:12639–45.
- [73] Panda, D.; Miller, H.; Islam, K.; Wilson, L. Stabilization of microtubule dynamics by estramustine by binding to a novel site in tubulin: a possible mechanistic basis for its antitumor action. *Proceedings of the National Academy of Science of the USA*, 1997, 94, 10560–10564.
- [74] Correia Faria, E.; Ma, N.; Gazi, E.; Gardner, P.; Brown, M.; Clarke N. W.; Snook, R.D. Measurement of elastic properties of prostate cancer cells using AFM. *Analyst*, 2008, 133:1498–1500.
- [75] Pillet, F.; Chopinet, L.; Formosa, C.; Dague, E. Atomic Force Microscopy and pharmacology: From microbiology to cancerology. *Biochimica et Biophysica Acta*, 2014, 1840:1028-1050.

- [76] Xu, K.; Schwarz, P. M.; Luduena, R. F. Interaction of Nocodazole With Tubulin Isoforms. *Drug Development Research*, 2002, 55:91-96.
- [77] Hoebeke, J.; Van Nijen, G.; De Brabander, M. Interaction of oncodazole (R 17934), a new anti-tumoral drug, with rat brain tubulin. *Biochemical and Biophysical Research Communications*, 1976, 69(2):319-324.
- [78] Jokhadar, S. Z.; Derganc, J. Structural Rearrangements in CHO Cells After Disruption of Individual Cytoskeletal Elements and Plasma Membrane. *Cell Biochemistry and Biophysics*, 2015, 71(3):1605-1613.
- [79] Kadi, A.; Pichard, V.; Lehmann, M.; Briand, C.; Braguer, D.; Marvaldi, J.; Rognoni, J.-B.; Luis, J. Effect of Microtubule Disruption on Cell Adhesion and Spreading. *Biochemical and Biophysical Research Communications*, 1998, 246(3):690-695.
- [80] Elineni, K. K.; Gallant, N. D. Microtubules Mechanically Regulate Cell Adhesion Strengthening Via Cell Shape. *Cellular and Molecular Bioengineering*, 2014, 7(1):136-144.
- [81] Wilson, L.; Toso, R. J.; Jordan, M. A. 1993. Vinblastine, Nocodazole, and colchicine suppress the dynamic instability of microtubules: Implications for the mechanism of antimitotic action. *Journal of Cell Pharmacology*, 1993, 1(Suppl. I):35-40.
- [82] Vasquez, R. J.; Howell, B.; Yvon, A. M. C.; Wadsworth, P.; Cassimeris, L. Nanomolar concentrations of Nocodazole alter microtubule dynamic instability in vivo and in vitro. *Molecular Biology of the Cell*. 1997, 8:973-985.
- [83] Guzman-Sepulveda, J. R.; Deng, J.; Fang, J. Y.; Dogariu, A. In situ characterization of structural dynamics in swelling hydrogels. *Soft Matter*, 2016, 12:5986-5994.
- [84] Guzman-Sepulveda, J. R.; Deng, J.; Fang, J.Y.; Dogariu, A. Characterizing Viscoelastic Modulations in Biopolymer Hydrogels by Coherence-Gated Light Scattering. *Journal of Physical Chemistry B*, 2017, 121:9234-9238.

- [85] Guzman-Sepulveda, J. R.; Argueta-Morales, R.; DeCampi, W. M.; Dogariu, A. Real-time intraoperative monitoring of blood coagulability via coherence-gated light scattering, *Nature Biomedical engineering*, 2017, 1:0028.
- [86] Berne, B. J.; Pecora, R. *Dynamic Light Scattering: With Applications to Chemistry, Biology, and Physics*. Courier Corporation, 1976.
- [87] Xu, R. Light scattering: A review of particle characterization applications. *Particuology*, 2015, 18:11-21.
- [88] Brown, G. M. Homodyne Optical Fiber Dynamic Light Scattering. *Applied Optics*, 2001, 20:4004–4010.
- [89] Benzhuo, L. Particle Sizing with PCS Mixed of Self-beating Mode and Heterodyne Mode. *Particle & Particle Systems Characterization*, 2008, 25:414–419.
- [90] Shetty, A. M.; Wilkins, G. M. H.; Nanda, J.; Solomon, M. J. Multiangle Depolarized Dynamic Light Scattering of Short Functionalized Single-Walled Carbon Nanotubes. *Journal of Physical Chemistry C*, 2009, 113(17):7129–7133.
- [91] Guzman-Sepulveda, J. R.; Dogariu, A. Probing complex dynamics with spatiotemporal coherence-gated DLS. *Applied Optics*, 2019, 58(13):D76-D90.
- [92] Popescu, G; Dogariu, A. Scattering of low coherence radiation and applications, *European Physical Journal Applied Physics*, 2005, 32:73–93.
- [93] Cummins, H.; Swinney, H. "Light beating spectroscopy". *Progress in Optics*, E. Wolf, ed. North-Holland, 1970, pp. 146–150.
- [94] Jakeman, E. "Photon correlation". *Photon Correlation and Light Beating Spectroscopy*. Springer, 1974, pp. 75–149.
- [95] Popescu, G.; Dogariu, A.; Rajagopalan, R. Spatially resolved microrheology using localized coherence volumes. *Physical Reviews E: Statistical, Nonlinear and Soft Matter Physics*, 2002, 65, 041504.
- [96] Sohn, I. S.; Rajagopalan, R.; Dogariu, A. Spatially resolved microrheology through a liquid/liquid interface. *Journal of Colloid Interface Science*, 2004, 269(2):503–513.

- [97] Liang, W.; Guzman-Sepulveda, J. R.; He, S.; Dogariu, A.; Fang, J. Microrheology and release behaviors of self-assembled steroid hydrogels. *Journal of Material Science and Chemical Engineering*, 2015, 3:6–15.
- [98] Rajagopalan, R.; Dogariu, A. Spatially resolved microrheology through a liquid/liquid interface. *Journal of Colloid Interface Science*, 2004, 269:503–513.
- [99] Guzman-Sepulveda, J. R.; Douglass, K. M.; Amin, S.; Lewis, N. E.; Dogariu, A. Passive optical mapping of structural evolution in complex fluids. *RSC Advances*, 2015, 5:5357–5362.
- [100] Mason, T. G. Estimating the viscoelastic moduli of complex fluids using the generalized Stokes–Einstein equation. *Rheological Acta*, 2000, 39:371–378.
- [101] Mason, T. G.; Weitz, D. Optical measurements of frequency dependent linear viscoelastic moduli of complex fluids. *Physical Review Letters*, 1995, 74:1250–1253.
- [102] Maggs, A.; Micro-bead mechanics with actin filaments. *Physical Review E*, 1998, 57:2091–2094.
- [103] MacKintosh, F.; Schmidt, C. Microrheology. *Current Opinion in Colloid & Interface Science*, 1999, 4:300–307.
- [104] Li, Q. S.; Lee, G. Y. H.; Ong, C. N.; Lim, C.T. AFM indentation study of breast cancer cells. *Biochemical and Biophysical Research Communications*, 2008, 374:609-613.
- [105] Kasas, S.; Ruggeri, F. S.; Benadiba, C.; Maillard, C.; Stupar, P.; Tournu, H.; Dietler, G.; Longo, G. Detecting nanoscale vibrations as signature of life. *Proceedings of the National Academy of Science of the USA*, 2015, 112(2):378-381.
- [106] Kim, K. S.; Cho, C. H.; Park, E. K.; Jung, M.-H.; Yoon, K.-S.; Park, H.-K. AFM-Detected Apoptotic Changes in Morphology and Biophysical Property Caused by Paclitaxel in Ishikawa and HeLa Cells. *PLOS ONE*, 2012, 7(1): e30066.

- [107] Iyer, S.; Gaikwad, R. M.; Subba-Rao, V.; Woodworth, C. D.; Sokolov, I. Atomic force microscopy detects differences in the surface brush of normal and cancerous cells. *Nature Nanotechnology*, 2009, 4:389-393.
- [108] Li, M.; Liu, L.; Xi, N.; Wang, Y. Nanoscale monitoring of drug actions on cell membrane using atomic force microscopy. *Acta Pharmacologica Sinica*, 2015, 36:769–782.
- [109] Rotsch, C.; Radmacher, M. Drug-Induced Changes of Cytoskeletal Structure and Mechanics in Fibroblasts: An Atomic Force Microscopy Study. *Biophysical Journal*, 2000, 78:520-535.
- [110] Longo, G.; Alonso-Sarduy, L.; Marques Rio, L.; Bizzini, A.; Trampuz, A.; Notz, J.; Dietler, G.; Kasas, S. Rapid detection of bacterial resistance to antibiotics using AFM cantilevers as nanomechanical sensors. *Nature Nanotechnology*, 2013, 8:522-526.
- [111] Stupar, P.; Podolski-Renic, A.; Villalba, M. I.; Dragoj, M.; Jovanovic Stojanov, S.; Pesic, M.; Kasas, S. Nano-Motion Analysis for Rapid and Label Free Assessing of Cancer Cell Sensitivity to Chemotherapeutics. *Medicina*, 2021, 57, 446.
- [112] Wu, S.; Liu, X.; Zhou, X.; Liang, X. M.; Gao, D.; Liu, H.; Zhao, G.; Zhang, Q.; Wu, X. Quantification of cell viability and rapid screening anti-cancer drug utilizing nanomechanical fluctuation. *Biosensor and Bioelectronics*, 2016, 77:164-173.
- [113] Johnson, W. L.; Cook France, D.; Rentz, N. S.; Cordell, W. T.; Walls, F. L. Sensing bacterial vibrations and early response to antibiotics with phase noise of a resonant crystal. *Scientific Reports*, 2017, 7, 12138.
- [114] Behera, B.; Anil Vishnu, G. K.; Chatterjee, S.; Sitaramgupta V, V. S. N.; Sreekumar, N.; Nagabhushan, A.; Rajendran, N.; Prathik, B. H.; Pandya, H. J. Emerging technologies for antibiotic susceptibility testing. *Biosensor and Bioelectronics*, 2019, 142, 111552.
- [115] Tannert, A.; Grohs, R.; Popp, J.; Neugebauer, U. Phenotypic antibiotic susceptibility testing of pathogenic bacteria using photonic readout methods:

- recent achievements and impact. *Applied Microbiology and Biotechnology*, 2019, 103:549–566.
- [116] Engelborghs, Y.; De Maeyer, L. C. M.; Overbergh, N. A kinetic analysis of the assembly of microtubules in vitro. *FEBS Letters*, 1977, 80(1):81-85.
- [117] Schmidt, M.; Kierfeld, J. Chemomechanical Simulation of Microtubule Dynamics With Explicit Lateral Bond Dynamics. *Frontiers in Physics*, 2021, 9, 673875.
- [118] Flyvbjerg, H.; Jobs, E.; Leibler, S. Kinetics of self-assembling microtubules: An "inverse problem" in biochemistry. *Proceedings of the National Academy of Science of the USA*, 1996, 93:5975-5979.
- [119] Henderson, M. A. The interaction of water with solid surfaces: fundamental aspects revisited. *Surface Science Reports*, 2002, 46(1-8):1-308.
- [120] Elton D. C.; Spencer, P. D.; Riches, J. D.; Williams, E. D. Exclusion Zone Phenomena in Water—A Critical Review of Experimental Findings and Theories. *International Journal of Molecular Science*, 2020, 21, 5041.
- [121] Zheng, J. M.; Pollack, G. H. Long-range forces extending from polymer-gel surfaces. *Physical Review E* 2003, 68, 031408.
- [122] Pollack, G. H. The Fourth Phase of Water: Beyond Solid, Liquid, and Vapor. *Edgescience*, 2013, 16:14-18.
- [123] Zheng, J. M.; Pollack, G. H. Solute Exclusion And Potential Distribution Near Hydrophilic Surfaces. *Water and the Cell*, 2006, 8.
- [124] Das, R.; Pollack, G. H. Charge-Based Forces at the Nafion–Water Interface. *Langmuir*, 2013, 29(8):2651-2658.
- [125] Chai, B.; Yoo, H.; Pollack, G. H. Effect of Radiant Energy on Near-Surface Water. *Journal of Physical Chemistry B* 2009, 113:13953–13958.
- [126] Wang, A.; Pollack, G. H. Effect of infrared radiation on interfacial water at hydrophilic surfaces. *Colloid and Interface Science Communication*, 2021, 42, 100397.
- [127] Mercado-Uribe, H.; Guevara-Pantoja, F. J.; Garcia-Munoz, W.; Garcia-Maldonado, J. S.; Mendez-Alcaraz, J. M.; Ruiz-Suarez, J. C. On the evolution of

- the exclusion zone produced by hydrophilic surfaces: A contracted description. *Journal of Chemical Physics*, 2021, 154, 194902.
- [128] Pokorný, J.; Pokorný, J.; Kobilková, J.; Jandová, A.; Vrba, J.; Vrba, J. Jr. Targeting Mitochondria for Cancer Treatment – Two Types of Mitochondrial Dysfunction. *Prague Medical Report*, 2014, 115(3–4):104–119.
- [129] Sommer, A. P.; Caron, A.; Fecht, H.-J. Tuning Nanoscopic Water Layers on Hydrophobic and Hydrophilic Surfaces with Laser Light. *Langmuir*, 2008, 24:635-636.
- [130] Sommer, A. P.; Hodeck, K. F.; Zhu, D.; Kothe, A.; Lange, K. M.; Fecht, H.-J.; Aziz, E. F. Breathing Volume into Interfacial Water with Laser Light. *Journal of Physical Chemistry Letters*, 2011, 2:562–565.
- [131] Passerella, S.; Casamassima, E.; Molinari, S.; Pastore, D.; Quagliarello, E.; Catalano, I. M.; Cingolani, A. Increase of proton electrochemical potential and ATP synthesis in rat liver mitochondria irradiated in vitro by helium-neon laser. *FEBS*, 1984, 175(1):95-99.
- [132] Sommer, A. P.; Haddad, M. Kh.; Fecht, H.-J. Light Effect on Water Viscosity: Implication for ATP Biosynthesis. *Scientific Reports*, 2015, 5, 12029.
- [133] Tyner, K. M.; Kopelman, R.; Philbert, M. A. “Nanosized Voltmeter” Enables Cellular-Wide Electric Field Mapping. *Biophysical Journal*, 2007, 93:1163–1174.
- [134] Preto, J.; Pettini, M.; Tuszynski, J. A. Possible role of electrodynamic interactions in long-distance biomolecular recognition. *Physical Review E*, 2015, 91, 052710.
- [135] Garvalov, B. K.; Zuber, B.; Bouchet-Marquis, C.; Kudryashev, M.; Gruska, M.; Beck, M.; Leis, A.; Frischknecht, F.; Bradke, F.; Baumeister, W.; Dubochet, J.; Cyrklaff, M. Luminal particles within cellular microtubules. *Journal of Cell Biology*, 2006, 174:759–765.
- [136] Coombes, C., Yamamoto, A.; McClellan, M.; Reid, T. A.; Plooster, M.; Gant Luxton, G. W.; Alper, J.; Howard, J.; Gardner, M. K. Mechanism of microtubule lumen entry for the  $\alpha$ -tubulin acetyltransferase enzyme  $\alpha$ TAT1.

- Proceedings of the National Academy of Science of the USA, 2016, 113:E7176–E7184.
- [137] Unger, E.; Boehm, K.; Vater, W. Structural Diversity and Dynamics of Microtubules and Polymorphic Tubulin Assemblies. *Electron Microscopy Reviews*, 1990, 3:355-395.
- [138] Chen, C.-S.; Chung, W.-J.; Hsu, I. C.; Wu, C.-M.; Chin, W.-C. Force field measurements within the exclusion zone of water. *Journal of Biological Physics*, 2012, 38:113–120.
- [139] Esplandiú, M. J.; Reguera, D.; Fraxedas, J. Electrophoretic Origin of Long-range Repulsion of Colloids near Water/Nafion Interfaces. *Soft Matter*, 2020, 16, 3717.
- [140] VanBuren, V.; Odde, D. J.; Cassimeris, L. Estimations of lateral and longitudinal bond energies within the microtubule lattice. *Proceedings of the National Academy of Science of the USA*, 2002, 99:6035–6040.
- [141] VanBuren, V.; Cassimeris, L.; Odde, D. J. Mechanochemical model of microtubule structure and self-assembly kinetics. *Biophysical Journal*, 2005, 89:2911–2926.
- [142] Tsenkova, R. Visible-Near Infrared perturbation spectroscopy: Water in action seen as a source of information. *Proceedings of the 12th International Conference on Near-infrared Spectroscopy*, Auckland, New Zealand, 9–15 April 2005; pp. 514–519.
- [143] Muncan, J.; Tsenkova, R. Aquaphotomics—From Innovative Knowledge to Integrative Platform in Science and Technology. *Molecules*, 2019, 24, 2742.
- [144] Tsenkova, R.; Muncan, J.; Pollner, B.; Kovacs, Z. Essentials of Aquaphotomics and Its Chemometrics Approaches. *Frontiers in Chemistry*, 2018, 6, 363.
- [145] Fahri, A.; Dogariu, A. Coupling of electrodynamic fields to vibrational modes in helical structures, *Physical Review A*, 2021, 103, 023523.
- [146] Lechelon, M.; Meriguet, Y.; Gori, M.; Ruffenach, S.; Nardecchia, I.; Floriani, E.; Kudashova, A.; Coquillat, D.; Teppe, F.; Mailfert, S.; Marguet, D.;

- Ferrier, P.; Varani, L.; Sturgis, J.; Torres, J.; Pettini, M. Experimental evidence for long-distance electrodynamic intermolecular forces. 2021, hal-03259009.
- [147] Sukhov, S.; Douglass, K. M.; Dogariu, A. Dipole–dipole interaction in random electromagnetic fields. *Optics Letters*, 2013, 38(14):2385-2387.
- [148] Tulub, A. A.; Stefanov, V. E. Activation of tubulin assembly into microtubules upon a series of repeated femtosecond laser impulses. *Journal of Chemical Physics*, 2004, 121(22):11345-11350.
- [149] Sommer, A. P.; Zhu, D.; Scharnweber, T. Laser modulated transmembrane convection: Implementation in cancer chemotherapy. *Journal of Controlled Release*, 2010, 148:131-134.
- [150] Huston, L. L.; Odell, J.; Lee, Y. C.; Himes, R.H. Solvent Isotope Effects on Microtubule Polymerization and Depolymerization, *Journal of Molecular Biology*, 1974, 87:141-146.